Separation and Transition on the ROTEX-T Cone-Flare

Jonathan Davami* and Thomas J. Juliano†
University of Notre Dame, Notre Dame, Indiana, 46556, USA

Anton Scholten‡
North Carolina State University, Raleigh, NC 27695, USA

Pedro Paredes§
National Institute of Aerospace, Hampton, VA 23666, USA

Elizabeth K. Benitez¶
U.S. Air Force Research Laboratory, Wright-Patterson AFB, OH 45433

Carson L. Running‖
University of Dayton, Dayton, Ohio, 45469, USA

Kamil Dylewicz**
University of Liverpool, The Quadrangle, Brownlow Hill, L69 3GH, UK

Vojtech Pezlar††
CTU Prague, Prague 16000, Czech Republic

Vassilis Theofilis‡‡
Technion-Israel Institute of Technology, Haifa 32000, Israel

Thomas Thiele§§ and Sebastian Willems¶¶
German Aerospace Center (DLR), Cologne, NRW 51147, Germany

As part of NATO STO AVT-346 "Predicting Hypersonic Boundary-Layer Transition on Complex Geometries," coordinated experimental and computational studies were conducted on the ROTEX-T, a cone-flare geometry used in a successful flight-test experiment. At the as-flown conditions, a separation bubble existed at the compression corner. Separation, reattachment, and the multifaceted linear instability paths leading this bubble to transition to turbulence are challenging to predict, but have significant impact on surface pressure and heat flux. High-resolution background-oriented schlieren and infrared thermography measurements were made in the AFOSR–Notre Dame Large Mach-6 Quiet Tunnel at freestream unit Reynolds numbers from 5.8×10^6 to 12.2×10^6 m^{-1} and nominally zero angle of attack. High-speed self-aligned focusing schlieren, infrared thermography, and focused laser differential interferometry measurements were made in the AFRL Mach-6 Ludwieg Tube from 2.2×10^6 to 24.7×10^6 m^{-1} and nominally zero degrees angle of attack. The surface heat-flux and Stanton number distributions were computed. Separation and reattachment locations, as well as the flow state

*Graduate Student, Department of Aerospace and Mechanical Engineering, Student Member, AIAA.
†Associate Professor, Department of Aerospace and Mechanical Engineering. Associate Fellow, AIAA. Corresponding author, tjuliano@nd.edu.
‡Graduate Student, Department of Mechanical and Aerospace Engineering. Student Member, AIAA.
§Associate Research Fellow, Computational AeroSciences Branch, NASA LaRC. Associate Fellow, AIAA.
¶Research Aerospace Engineer, Aerospace Systems Directorate. AIAA Member.
‖Assistant Professor, Department of Mechanical and Aerospace Engineering. AIAA Member.
**Graduate Student, School of Engineering, Student Member, AIAA
††Graduate Student, Student Member, AIAA
‡‡Professor, Faculty of Aerospace Engineering, Associate Fellow, AIAA
§§Research Aerospace Engineer, Supersonic and Hypersonic Technologies Department
¶¶Research Aerospace Engineer, Supersonic and Hypersonic Technologies Department

at each, were determined from the combination of surface and off-wall measurements. The convective and global boundary-layer instabilities of the axisymmetric laminar flow at the experimental conditions were investigated computationally. Amplification of Mack's first and second modes were observed to have logarithmic amplification factors between 5 to 7.5 at the separation location, depending on conditions. The flow was found to be globally unstable to stationary three-dimensional disturbances concentrated in the reattachment region.

Previous analysis of the ROTEX-T flight data had not assessed reattachment location or the flow state upon reattachment. Thanks to the insights gained from the coordinated, on- and off-wall ground-test measurements, these evaluations have now been made. The separation location indicated by laminar simulations is consistently numerically predicted to be upstream of the experimentally observed location for a transitional separation bubble. The cause of this difference is understood to lie in the steady-state and axisymmetric assumptions made by both solvers employed to compute the basic states analyzed, as flow topology considerations assert that unsteady two-dimensional or axisymmetric separation bubbles are structurally unstable and will become three-dimensional. Computed laminar heating rates prior to separation agreed well with experiment; transitional heating rates after reattachment were between laminar and turbulent computations.

Nomenclature

A	Amplitude
c_p	Specific heat at constant pressure
h	Enthalpy
L	Cone length
M	Mach number
m	Wavenumber
p	Pressure
$\dot{q}''$	Heat flux
Re_∞	Freestream unit Reynolds number
Re_L	Reynolds number based on the cone length, L
St	Modified Stanton number
T	Temperature
u	Velocity
x	Streamwise distance
y	Centerline-normal distance
α	Angle of attack
β	Side-slip angle
δ	Boundary-layer thickness
δ_θ	Boundary-layer momentum thickness
σ	Growth rate
ρ	Density
ϕ	Azimuthal angle
θ	Polar angle

Subscripts

0	Stagnation
∞	Freestream
e	Boundary-layer edge
n	Nose
r	Reattachment
s	Separation
w	Wall

I. Introduction

Shock-wave/boundary-layer interactions (SWBLIs) increase the difficulty of analyzing viscous compressible flows. Large pressure variations and intense surface heating are major concerns [1, 2]. The interaction between shock waves and boundary layers often causes boundary layers to transition, a notable consequence since transitional and turbulent boundary layers engender heating rates several times larger than laminar boundary layers, and ten times larger than in separated regions [1, 3, 4]. Therefore, the prediction of boundary-layer transition and separation is critical for the design of hypersonic vehicles [5–9]. Modeling hypersonic SWBLIs to predict separation and reattachment, heat transfer, skin friction, unsteadiness, and viscous-inviscid interactions has been challenging [7, 10, 11].

Researching SWBLIs requires a geometry that is not too complex for collaborative efforts among computationalists, experimentalists, and flight test engineers [2, 10, 12, 13]. Hence, an emphasis has been placed on interactions with thick, well-defined boundary layers in which three-dimensional effects are not overwhelming [1, 3, 4, 14, 15]. The hollow cylinder/flare is one such well-documented configuration [3, 15–17]. Cone-flares (i.e., double cones) and cone-cylinder-flares are also common [1, 4, 14, 18–25].

A cone-flare geometry is used in the present study. The boundary layer approaching the compression corner depends on the freestream conditions, surface roughness, surface temperature, cone angle, and nose radius. The state of the boundary layer significantly influences the interaction. Laminar boundary layers are prone to separate due to the adverse pressure gradient imposed by the flare. If the boundary layer separates, a separation shock will form. Boundary-layer reattachment will occur on the flare if it is long enough, leading to a reattachment shock. High heating rates occur post reattachment as a result of a thin boundary layer and high density [4]. Between separation and reattachment, a recirculation bubble forms. An expansion wave forms at the intersection of the separation and reattachment shocks as the flow turns parallel to the flare [26]. This is a type VI interference from the Edney shock-shock classifications [6].

In addition to their sensitivity to upstream instabilities that can influence the state of the incoming boundary layer, compression-corner flows exhibit instabilities that affect downstream development. For example, they can cause transition prior to amplification of the second Mack mode [27]. Balakumar et al. performed a computational analysis on a 5.5° compression corner to study the evolution of the second mode, revealing three distinct regions [27]. The first region is upstream of separation, where disturbances grow in accordance with the linear theory of self-similar boundary layers. In the second region, disturbances remain neutral, residing above the separation bubble and without penetrating the separated region. The third region is downstream of the separation bubble, where disturbances once again exhibit exponential growth. Focused Laser Differential Interferometry (FLDI) measurements on a cone-cylinder-flare indicated instabilities could be generated or amplified by the bubble's shear layer [14, 24, 25]. A spectral proper orthogonal decomposition (SPOD) analysis of high-speed schlieren images for a hollow-cylinder-flare also identified oblique shear-layer modes as the dominant instability [15]. Other recent experiments used global bispectral analysis and SPOD on ultra-high-speed schlieren and surface pressure measurements for global frequency-domain analysis for a cone-flare at freestream unit Reynolds numbers from 3.3×10^6 to 5.2×10^6 m^{-1} with flare half-angles of 5°, 10°, and 15° [22]. For the 15° flare, disturbances in the separated shear layer exhibited much larger N-factors than second-mode waves.

II. Flight-Test Synopsis

The Rocket Technology Experiment–Transition (ROTEX-T) was a low-cost, two-stage sounding rocket flight test performed by the German Aerospace Center (DLR) [28]. It was launched successfully on July 19, 2016, from the Esrange Space Center in northern Sweden. ROTEX-T built upon the experience gained during the SHEFEX-I and -II flight tests [12, 29, 30]. The design of the experiment and analysis of the data were supported by students of the RWTH Aachen University. The ROTEX-T payload consisted of a 7° half-angle circular cone with a nose radius of 2.5 mm followed by a 20° half-angle flare (Figs. 1, 2).

Fig. 1 Photograph of the ROTEX-T payload mounted to the second stage [Source: DLR].

The instrumentation was arrayed along four lines 90° apart azimuthally. It includes surface pressure measurements with Kulite® XTE-190M transducers (KU) and PCB® 132A31 sensors (PCB) as well as heat-flux measurements with type 7E/H heat flux microsensors (HFM) and coaxial thermocouples (TC) (Fig. 3). The TC and HFM sensors compared herein were all along the ϕ = 90° and ϕ = 270° rays. The transformation of the surface temperature signal of the coaxial thermocouples to heat flux was based on the one-dimensional heat equation.

Since ROTEX-T did not include an inertial measurement unit (IMU), the altitude and velocities of the trajectory reconstruction are based on GPS data. The freestream pressure and temperature data were derived from balloon measurements and the CIRA-86 atmosphere model [32]. The angle of attack and side-slip angle were calculated based on four surface pressure measurements spaced circumferentially around the cone. A detailed description of the instrumentation and the post processing of the flight data is given in Ref. [31].

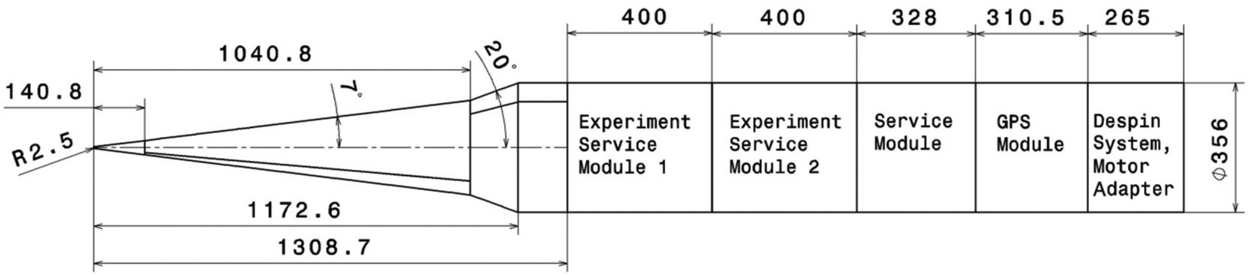

Fig. 2 Dimensions of the ROTEX-T payload.

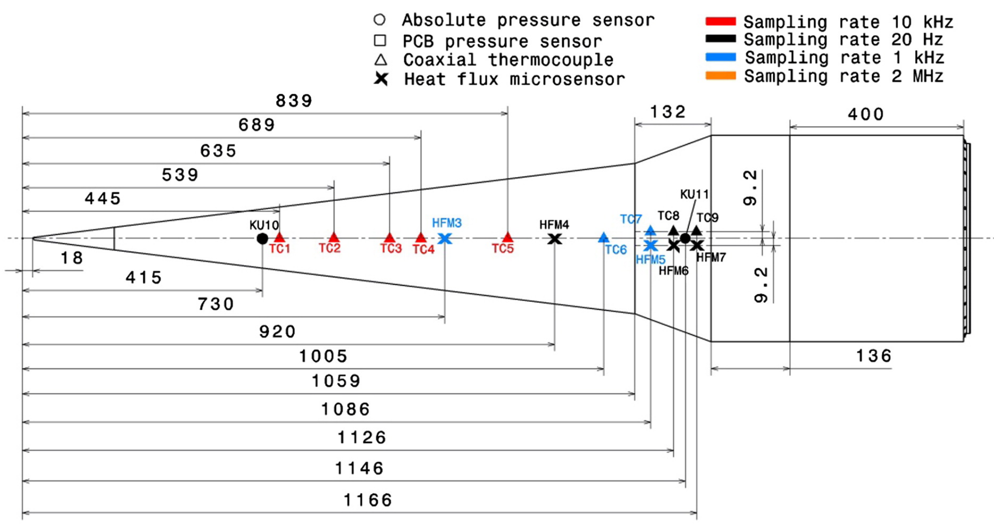

(a) $\phi = 90°$**. (Fig. 11 in Ref. [31].)**

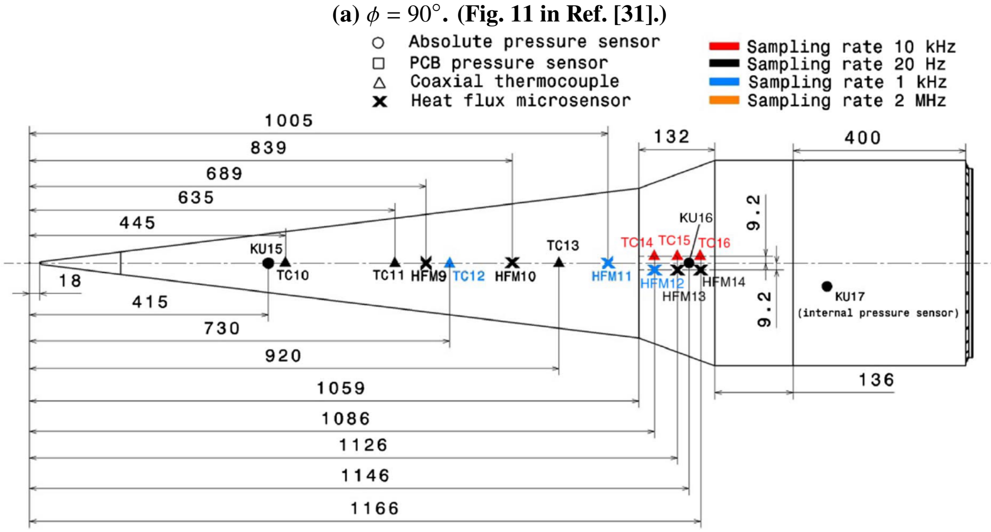

(b) $\phi = 270°$**. (Fig. 13 in Ref. [31].)**

Fig. 3 Flight instrumentation.

The flight vehicle achieved a maximum Mach number of 5.1 during ascent to an apogee of 183 km, followed by a maximum Mach number of 5.5 during reentry. There was a Yo-Yo despin system on the payload, but no attitude control. Therefore, the descent started with very high angles of attack, and realignment was solely via aerodynamics. Thus, the majority of the heating analysis was focused on ascent, which experienced very small angles of attack.

III. Ground-Test Model & Facilities

A. Model

The test article is a 39% scale model of the ROTEX-T payload (Fig. 4, Table 1). (The unusual scale was chosen to reuse previously fabricated hardware.) The model consisted of three main components: nose tip, frustum, and a set of four flare petals. The nose tips were fabricated from stainless steel. Three nose radii were tested: 0.99 mm (39% scale), 0.01 mm (sharp), and 5 mm (blunt). The flare and frustum are aluminum. The same model was used in the test campaigns at both the University of Notre Dame and the Air Force Research Laboratory.

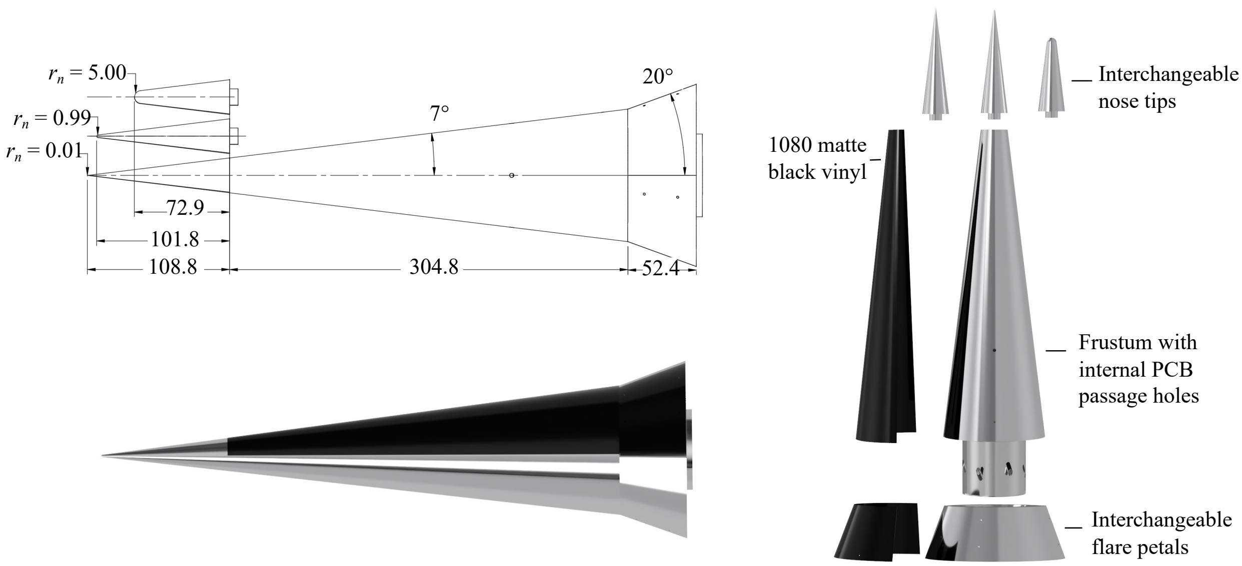

Fig. 4 Test article drawing, assembly, and exploded view. Dimensions are in millimeters.

Table 1 Full-scale ROTEX-T and model dimensions.

Dimension (mm)	Full-scale	39% scale	Sharp nose	Blunt nose
Nose radius (r_n)	2.5	0.99	0.01	5.00
Conical body length (L)	1040.8	406.6	413.6	377.7
Entire model length (L_Model)	1172.6	459.0	466.0	430.1
Junction diameter (d)	260.1	101.6	101.6	101.6

B. ANDLM6QT

Experiments were conducted in the Air Force Office of Scientific Research–Notre Dame Large Mach-6 Quiet Tunnel (ANDLM6QT). The facility is a Ludwieg tube with a 60 m-long driver tube [33]. Heating blankets on the driver tube permit stagnation temperatures from 435 to 590 K. A valve at the contraction exit opens to start a run, which lasts ≈ 1 s. The expansion wave generated at the start of each run undergoes multiple reflections within the driver tube before the tunnel unstarts. With each reflection, the stagnation pressure and freestream unit Reynolds number decrease by less than 10%. The flow is approximately steady during the intervals between reflections. The experiment was conducted under conventional noise conditions ($p'/\overline{p}$ = 2.6%), with a freestream Mach number of 5.7 [34].

A schematic of the experimental setup is shown in Fig. 5. Infrared thermography (IR) and background-oriented schlieren (BOS) data were collected simultaneously. The IR camera was placed on the top of the tunnel, viewing the model's upper surface through an 8 mm thick calcium fluoride (CaF_2) window with a 70 mm viewing diameter and transmission range of 0.15–9.0 μm. The viewing distance was 585 mm. The high-resolution camera, used for the BOS measurements, viewed through a 127 mm diameter acrylic window on the test section left door. The viewing distance of the camera was 600 mm. The BOS background was placed on the other side of the test section, behind a 457 mm diameter acrylic window. The BOS field of view was coincident with the IR camera. The model nose was 100 mm upstream of the nozzle exit plane.

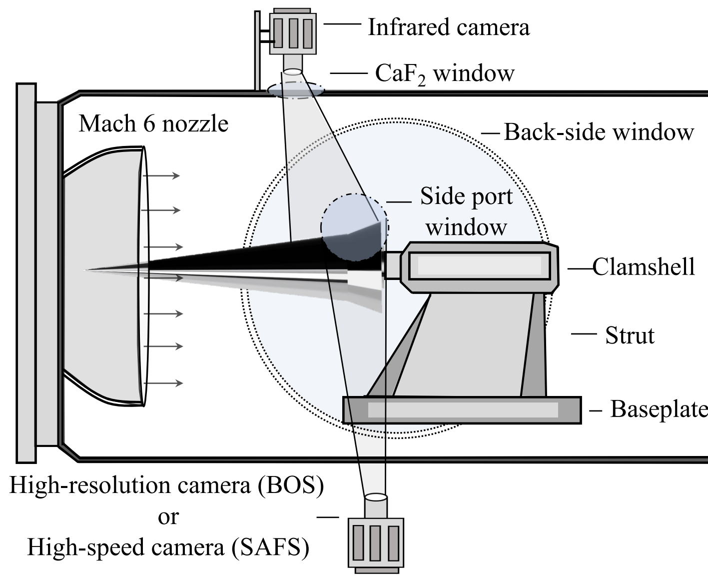

Fig. 5 Schematic of experimental setup.

Alignment with the freestream flow was established in each facility by measuring the frequency of second-mode waves with the sharp nose installed [35]. Four PCB132B38 sensors were positioned 8.9 mm upstream of the corner at 90-degree intervals around the azimuth. Based on the last adjustment made, both pitch and yaw alignment are within 0.0 ± 0.2°. Five Re_∞ conditions matching previous test campaigns were tested for each nose radius: p_0 = 490 ± 7 to 1014 ± 8 kPa, T_0 = 435 ± 3 K, and $Re_\infty = (5.8 \pm 0.1) \times 10^6$ to $(12.2 \pm 0.1) \times 10^6$ m^{-1} [23]. Freestream quantities were computed using isentropic relations with M_∞, P_0, and T_0. Sutherland's law was used to compute viscosity [36].

C. AFRL M6LT

The Air Force Research Laboratory Mach 6 Ludwieg Tube (AFRL M6LT) is equipped with a 30-inch diameter Mach 6 nozzle. The driver tube is built in two parallel 10.7 m sections connected by a 180° bend (i.e., a reflexed driver tube). It is wrapped with blanket resistance heaters over its entire length. A fast valve, comprising a large aluminum piston, initiates a run. Each run has a total duration of 0.2 seconds and consists of two approximately 0.1-second periods of quasi-steady flow, each period with a different Re_∞. The facility operates under conventional noise conditions ($p'/\overline{p} \approx 3\%$).

IR thermography, high-speed self-aligned focusing schlieren (SAFS), and linear-array focused laser differential interferometry (LA-FLDI) measurements were made. IR Thermography and SAFS measurements were collected simultaneously, while LA-FLDI measurements were taken separately. All data were collected on the upper surface of the model. The IR camera was positioned atop the tunnel, observing through a calcium fluoride window, while a Photron SA-Z high-speed camera was positioned to observe through a side port window. The model nose was 50 mm upstream of the nozzle exit plane. The same procedure was used to align with the freestream flow. Based on the last adjustment made, both pitch and yaw alignment are estimated to be within 0.0 ± 0.2°. Test conditions were: p_0 = 252 ± 7 to 2673 ± 15 kPa, T_0 = 460 ± 3 K, and $Re_\infty = (2.2 \pm 0.1) \times 10^6$ to $(24.7 \pm 0.1) \times 10^6$ m^{-1}.

IV. Instrumentation

A. Infrared Thermography

Due to low aluminium emissivity, 3M 1080 matte black vinyl self-adhesive film was applied to a 180-degree sector of the model frustum and flare for improved IR thermography [37]. The model surface temperature was measured using two InfraTech midwave IR cameras, a 14-bit ImageIR 8300 hp (in the ANDLM6QT) and 16-bit ImageIR 9400 hp (in the AFRL M6LT). A 25 mm focal length lens and corresponding factory calibrations were used for both cameras. The resolution for both was 640×512 pixels, while the frame rates were 355 fps (ANDLM6QT) and 720 fps (AFRL M6LT). The cameras have an accuracy and resolution of ±1.0 K and 0.02 K (0.03 K for the ImageIR 9400), respectively. The maximum uncertainty of the measured surface temperature is ±0.3% for any given test [38, 39].

A perspective transformation matrix was computed to map the temperature distributions from the thermographs. Heat flux was calculated by solving the transient one-dimensional heat equation through space and time, for which the Fortran QCALC subroutine was translated to MATLAB [40]. QCALC assumes one-dimensional heat transfer and uses a second-order Euler explicit finite difference approximation to solve for the temperature distribution through the wall; heat flux is obtained from a second-order approximation to the derivative of the temperature profile at the outer surface [41]. The cylindrical-geometry equation was used with the local radius of curvature, thickness, and material properties of the vinyl wrap and underlying aluminum wall [42]. The initial condition is based on the assumption of a uniform through-wall temperature distribution, equal to the prerun surface temperature at each pixel. The measured surface temperature was applied as the front-face boundary condition. An adiabatic back-face boundary condition was applied. Radiation was neglected due to the relatively low temperatures. Lateral heat conduction was neglected.

The heat flux was converted to the nondimensional heat flux, the Stanton number. Throughout this work, a modified Stanton number is used:

$$St = \frac{\dot{q''}_{\mathrm{w}}}{c_p \rho_\infty u_\infty \left(T_0 - T_{\mathrm{w}}\right)} \quad , \tag{1}$$

where $\dot{q''}_{\mathrm{w}}$, c_p, ρ_∞, u_∞, T_0 and T_{w} are the heat flux, specific heat capacity of air at constant pressure, freestream density, freestream velocity, stagnation temperature, and wall temperature. The freestream quantities were computed using isentropic relations with the measured stagnation pressure, stagnation temperature, and Mach number. The standard heat capacity of air at constant pressure, 1004 J/kg·K, was assumed. The uncertainty in St was computed by analyzing and propagating the uncertainty associated with each of the parameters in Eq. 1, which were combined in quadrature. The net uncertainty of Stanton number is +10/−8%.

B. Background Oriented Schlieren

The BOS setup consisted of a camera, background, and two LED arrays. A Canon EOS RP mirrorless camera with a 24–105 mm F4 IS USM RF lens photographed the background. It has a 26.2 megapixel full-frame CMOS sensor and recorded video at 24 fps. A MATLAB function was used to generate a 210×297 mm white background filled with randomly distributed dots [43]. Two sheets covered the 0.41 m-diameter right-side acrylic window (Fig. 5). Each sheet had 200,000 dots with 0.25 mm diameter. With these background parameters and a video resolution of 3840×2160 pixels, the resulting particle diameter is 2.3 pixels. The particle density is 321 particles/cm^2. The speckled background was illuminated continuously with two GVM industrial LED light arrays.

The images were analyzed using the cross-correlation algorithm in PIVlab [13, 44, 45]. Four passes were performed with interrogation windows 64×64, 32×32, 16×16, and 8×8 pixels. This combination of image resolution and window sizes yields a 512×512 grid of displacement vectors, a physical resolution of 0.3 mm. To reduce noise, two consecutive displacement fields — collected 0.08 s apart — were averaged together. Since the flow field is nominally axisymmetric, the Filtered Back Projection Technique was used to obtain a center plane displacement field [46–49]. The density field was computed by solving the two-dimensional Poisson equation [20, 47, 50]. Neumann boundary conditions were prescribed at all boundaries [50]. Uncertainty quantification for BOS follows the procedure in Ref. [20]. The maximum uncertainty in displacement is ±0.026 pixels (±0.21 mm), corresponding to a maximum density uncertainty of ±0.01 kg/m^3, similar to previous studies [20, 51].

C. High-Speed Self-Aligned Focusing Schlieren

Schlieren imaging was used to both visualize the average bubble geometry as well as study the instabilities along the shear layer and reattached boundary layer. A Photron Fastcam SA-Z-2100K-M-32GB high-speed camera captured the images from a self-aligned focusing schlieren (SAFS) apparatus [52]. The focusing aspect of SAFS decreases the integration length of the schlieren, allowing the fluctuations from the tunnel shear layers to be reduced relative to the flow over the model. Lighting was provided by a Cavitar Cavilux HF 640 nm laser, with pulse lengths of either 100 or 30 ns depending on the frame rate. Images were taken at frame rates of 30 and 630 kHz, with higher frame rates achieved by reducing the viewing window size. Spectral proper orthogonal decomposition (SPOD) was used to analyze the high-frame-rate cases to better visualize any present instabilities [53].

D. Linear Array Focused Laser Differential Interferometry

Focused laser differential interferometry (FLDI) is a common-path interferometry technique that uses two closely spaced beams focused at the point of interest to estimate density fluctuations [54]. The technique takes advantage of the relationship between a fluid refractive index and density [55]. It measures the phase change that occurs between the beams by letting them interfere after passing through the gas and measuring the resulting beam intensity with either a photodetector or a high-speed camera. Linear array FLDI (LA-FLDI) extends the FLDI concept by splitting the beam several times to obtain multiple simultaneous density difference measurements [56]. More information about the technique and the specific apparatus used for this test can be found in Ref. [57].

A Thorlabs BC106N-VIS CCD beam profiler was used to measure the spacing between each individual beam. The beam array was oriented to be perpendicular to the cone surface. The beam pairs were 2141 μm apart in the streamwise direction and 548 μm apart vertically. The individual beams in each pair were separated by about 129 μm. The array was initially aligned with the model surface and traversed vertically until it passed through the separation shock. A Photron Fastcam SA-Z-2100K-M-32GB high-speed camera was used to collect the data with a frame rate of 900 kHz.

V. Primary Test Conditions

Flight-test, ground-test, and computational results were compared at two primary conditions, one each centered on ANDLM6QT and AFRL M6LT conditions (Table 2). The conditions were selected because the boundary layer entering into the SWBLI was laminar in flight (Figs. 30–32 in Ref. [31]). The Reynolds number based on cone length was matched for the flight and ground tests. The as-flown M_∞ at these Re_L are somewhat less than the tunnel conditions, 4.68 and 4.61 instead of 5.7 and 6.14. Flight data during ascent were used because more sensors were functional than during descent.

Table 2 Primary conditions for comparison.

L (m)	r_n (mm)	M_∞	Re_∞ ($\times 10^6$ m^{-1})	Re_L ($\times 10^6$)	α (°)	β (°)	Instrumentation
ANDLM6QT Comparison							
0.407	0.99	5.7	5.8	2.4	0	0	IR and BOS
1.041	2.50	4.68	2.3	2.4	−1.2	0.5	Flight
AFRL M6LT Comparison							
0.407	0.99	6.14	6.8	2.8	0	0	IR, SAFS, and LA-FLDI
1.041	2.50	4.61	2.7	2.8	0.5	−0.7	Flight

VI. Computational Results

A. Mean-Flow Solution

Computational results were obtained using the VULCAN-CFD* and SU2† solvers. VULCAN-CFD is a second-order-accurate, finite-volume algorithm for compressible Navier–Stokes [58–60]. The laminar-flow solutions obtained with this code were computed on a grid with 1601 × 601 points along the streamwise and wall-normal directions,

*Visit `http://vulcan-cfd.larc.nasa.gov` for further information about the VULCAN-CFD solver.
†Visit `https://su2code.github.io/` for further information about the SU2 solver.

respectively. The VULCAN-CFD solution is based on the full Navier–Stokes equations and uses the solver built-in capability to iteratively adapt the computational grid to the bow shock, boundary layer, and reattachment shock [61]. The adaptation process ensures enough points are clustered next to the model surface to resolve the thickness of the boundary layer within the separation region, as well as aligning the grid to the shocks. For the adaptation process, the boundary-layer edge is defined as the wall-normal position where $h_0/h_{0,\infty} = 0.99$, with h_0 denoting the total enthalpy, i.e., $h_0 = h + 0.5(\bar{u}^2 + \bar{v}^2 + \bar{w}^2)$, where $h = c_p\bar{T}$ is the static enthalpy. An offset is also applied and ensures the chosen number of cells in the wall normal direction will properly resolve the entropy layer as well. Sutherland's law for air is used to calculate the dynamic viscosity as a function of temperature.

An isothermal wall with $T_w^* = 290$ K and $T_w^* = 330$ K was used for the wind tunnel and flight conditions, respectively. Freestream conditions were selected to replicate both ground and flight tests (Table 3). The Mach number contours of two representative basic-state solutions, computed using VULCAN-CFD, are given in Fig. 6. In addition to the laminar solutions, fully-turbulent solutions were computed at the same freestream Reynolds numbers using the Menter-SST Reynolds-averaged Navier-Stokes (RANS) turbulence model [62] to compare with experimental results. Additional details of the implementation of the model in the VULCAN-CFD solver are found in Refs. [59, 60].

Table 3 Computational flow conditions.

	Re_∞ ($\times 10^6$ m^{-1})	r_n (mm)	u_∞ (m/s)	ρ_∞ (kg/m^3)	T_∞ (K)	T_0 (K)	T_w (K)	P_0 (kPa)
ANDLM6QT	5.79	0.99	872.35	0.0255	58.282	437.00	290	492.94
AFRL M6LT	6.75	0.99	901.26	0.0261	53.613	457.85	290	732.08
Flight	2.2675	2.5	1446.24	0.0241	238.075	1279.00	330	591.90
Flight	2.6529	2.5	1421.59	0.0285	236.236	1241.97	330	644.03

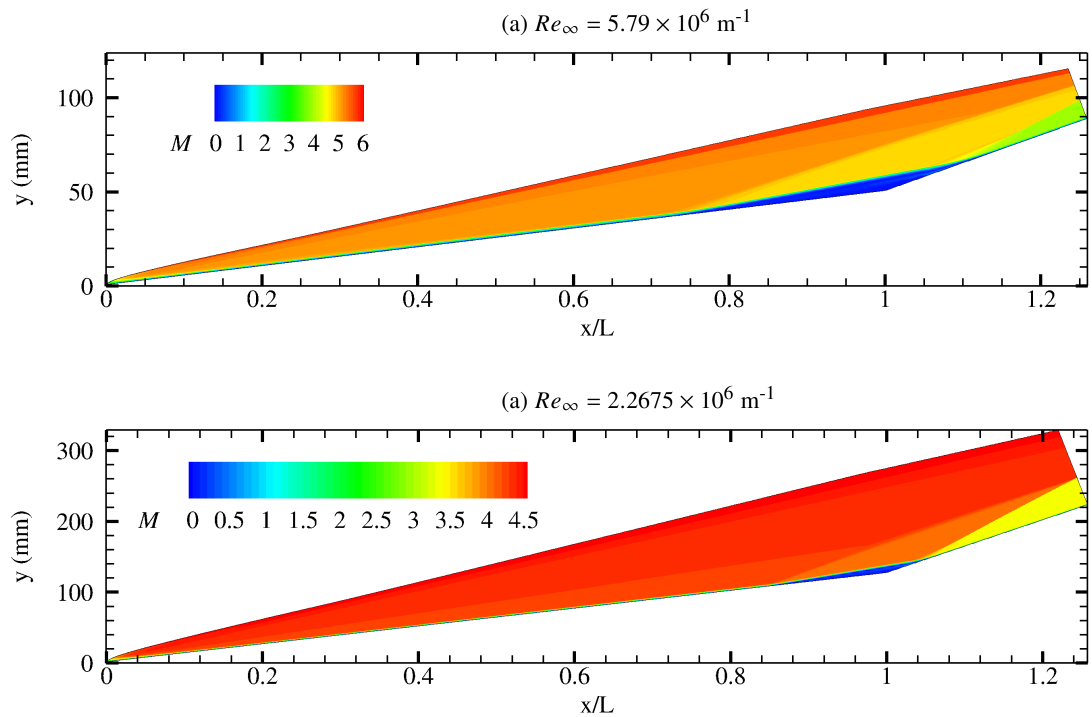

Fig. 6 Mach contours at the (a) wind tunnel and (b) flight conditions matching the ANDLM6QT. Steady laminar solutions computed with VULCAN-CFD.

SU2 is a second-order, finite-volume and finite-element solver for the compressible Navier–Stokes equations. Here, the laminar axisymmetric flow was computed on a static grid of 13800 × 1200 nodes with clustering toward the wall.

The inviscid terms were solved using the AUSM+–up algorithm and the the Venkatakrishnan slope-limiting method [63]. Convergence of the local time-stepping done with the implicit Euler scheme was accelerated using three multigrid levels. With SU2, only the 39% scale ROTEX-T model was considered, at conditions corresponding to $Re_\infty = 5.79 \times 10^6$ m^{-1}.

Both solvers used a steady-state algorithm to solve the flow. This achieves a numerically stable solution at relatively low residual convergence. However, for test cases where the reattachment is unsteady, this computational strategy violates flow physics of laminar separation [64–66] by preventing breakdown of the laminar separation bubble and forcing the flow to remain steady in the entire domain. This inability of steady-state algorithms to accurately capture the unsteady dynamics of separation and reattachment is likely to cause discrepancies with experimental results; such differences are discussed in Section VIII.

Profiles of wall-parallel velocity and density extracted from the VULCAN-CFD and SU2 simulations at $x/L = 0.592$, well upstream of separation, are shown in Fig. 7 (a) and (c) for $Re_\infty = 5.79 \times 10^6$ m^{-1}. For comparison, a self-similar, axisymmetric, zero-pressure-gradient, compressible boundary layer was computed ('BL' in the legend). The pertinent Illingworth-Levy-Lees transformation [67–69] was used, and the system of governing equations was solved iteratively using Runge-Kutta-Merson and Newton-Raphson methods. The momentum thickness, $\delta_\theta = 1.18 \times 10^{-4}$ m, of the self-similar boundary layer is used to normalize the vertical axis. Velocity and density are normalized by their boundary-layer edge values (subscript 'e'). Subfigures 7 (b) and (d) show velocity and density profiles at $x/L = 0.984$, after separation; the bow and separation shocks are both clearly visible. Within the separation region, the separation bubble length obtained from SU2 is used for normalization (see below). Good agreement is obtained between the SU2, VULCAN-CFD, and (where applicable) self-similar solutions. The most notable differences occur within the recirculation region, where SU2 predicts a sharper change of flow properties across the separation shock.

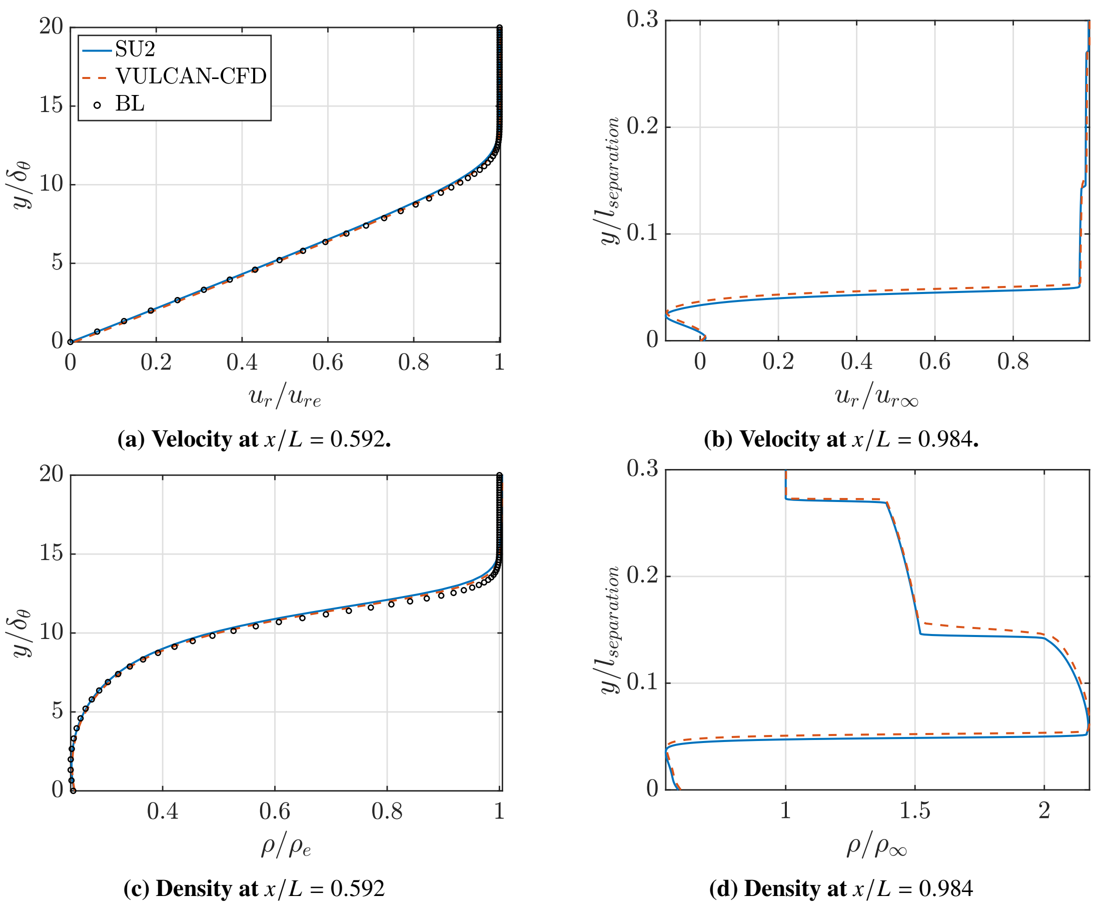

(a) Velocity at $x/L = 0.592$.

(b) Velocity at $x/L = 0.984$.

(c) Density at $x/L = 0.592$

(d) Density at $x/L = 0.984$

Fig. 7 Normalized profiles of the wall-parallel velocity component (u_r**) and density (**ρ**) upstream of separation (**$x/L = 0.592$**, subfigures a and c) and downstream of it (**$x/L = 0.984$**, subfigures b and d).**

The generalized inflection point (GIP) [70–73] is a compressible extension of Rayleigh's necessary, but not sufficient, condition for the existence of inviscid instabilities [74, 75]. For compressible, laminar boundary layers, the generalized inflection point is defined to be where $\partial_y(\rho\partial_y u) = 0$. Since this metric is associated with inviscid instabilities, comparison of its profiles between VULCAN-CFD, SU2, and theoretical solutions provides an insight into – and comparison between – stability properties of each boundary layer profile. Figure 8 presents $\partial_y(\rho\partial_y u)$ curves obtained from the two Navier-Stokes simulations and boundary-layer theory. The agreement is very good, with the inflection point at $y/\delta_\theta \approx 2.4$ and $y/\delta_\theta \approx 10$ matching very well, showing that VULCAN-CFD and SU2 resolve the laminar boundary layer upstream of the separation region. Moreover, the profiles from nonlinear simulations exhibit similar instability properties to the theoretical boundary layer profile.

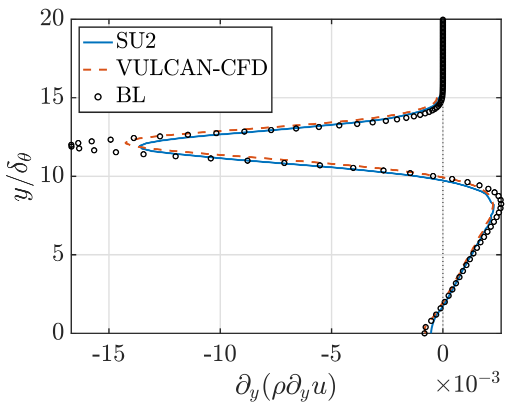

Fig. 8 Generalized inflection point of the laminar boundary layer upstream of separation ($x/L = 0.592$).

Separation bubble properties from the SU2 and VULCAN-CFD solutions are given in Table 4. Consistent values for the separation point are obtained by both solvers. Slightly different reattachment locations are obtained, leading to 7% difference in the respective predictions of the separation bubble length. The relative discrepancy between the two codes in their prediction of the normalized maximum reverse velocity is 6%.

Table 4 Separation bubble properties.

Code	$Re_\infty \times 10^6$ (m^{-1})	x_s (m)	x_s/L	x_r (m)	x_r/L	$l_{\text{separation}}$ (m)	$l_{\text{separation}}/L$	$\max(-u)/u_\infty$
SU2	5.79	0.3085	0.7587	0.4545	1.1180	0.1460	0.359	0.215
VULCAN-CFD	5.79	0.3038	0.7479	0.4574	1.1261	0.1536	0.3782	0.2280
	6.75	0.3007	0.7404	0.4575	1.1264	0.1568	0.3861	0.2316
	2.27	0.8718	0.8522	1.0832	1.0588	0.2114	0.2066	0.4607
	2.65	0.8676	0.8481	1.0815	1.0572	0.2139	0.2091	0.2029

B. Stability Analysis

The methodologies used for the analysis of disturbance amplification are equivalent to those used by Paredes et al. [76, 77] and Davami et al. [23]. The evolution of convective instabilities is calculated with the linear parabolized stability equations (PSE) and the harmonic linearized Navier-Stokes equations (HLNSE) frameworks. The global stability analysis (GSA) of the laminar flow solution is also performed.

The Cartesian coordinates are represented by (x, y, z). The computational coordinates are defined as an orthogonal body-fitted coordinate system along the cone region, with (ξ, η, ζ) denoting the streamwise (i.e., tangent to the cone), wall-normal, and azimuthal coordinates, respectively, and (u, v, w) representing the corresponding velocity components in the cone region. The same orientation of the coordinate system and velocities is maintained along the flare region with a nonorthogonal transformation of the two-dimensional grid. The density and temperature are denoted by ρ and T, respectively. The vector of basic state variables corresponds to $\bar{\mathbf{q}}(\xi, \eta, \zeta) = (\bar{\rho}, \bar{u}, \bar{v}, \bar{w}, \bar{T})^T$ and the vector of perturbation variables is denoted by $\tilde{\mathbf{q}}(\xi,\eta,\zeta,t) = (\tilde{\rho},\tilde{u},\tilde{v},\tilde{w},\tilde{T})^T$. For axisymmetric geometries at zero degrees angle of attack, the basic state variables are independent of the azimuthal coordinate, and the linear perturbations can be assumed to be harmonic in time and in the azimuthal direction, which leads to the following expression for the perturbations,

$$\tilde{\mathbf{q}}(\xi,\eta,\zeta,t) = \check{\mathbf{q}}(\xi,\eta)\exp\left[\mathrm{i}\,(m\zeta-\omega t)\right] + \text{c.c.}, \tag{2}$$

where the vector of disturbance functions is $\check{\mathbf{q}}(\xi,\eta,\zeta) = (\check{\rho},\check{u},\check{v},\check{w},\check{T})^T$, m is the azimuthal wavenumber, ω is the angular frequency, and c.c. refers to the complex conjugate.

The disturbance functions $\check{\mathbf{q}}(\xi,\eta,\zeta)$ satisfy the HLNSE [78], which involve coefficient functions that depend on the basic state variables and parameters, and on the angular frequency and azimuthal wavenumber of the perturbation,

$$\mathbf{L}_{\text{HLNSE}}\,\check{\mathbf{q}}(\xi,\eta) = \check{\mathbf{f}}, \tag{3}$$

where $\check{\mathbf{f}}$ represents a potential forcing term.

The PSE approximation to the HLNSE is based on isolating the rapid phase variations in the streamwise direction by introducing the disturbance ansatz

$$\check{\mathbf{q}}(\xi,\eta,\zeta) = \hat{\mathbf{q}}(\xi,\eta,\zeta)\exp\left[\mathrm{i}\int_{\xi_0}^{\xi}\alpha(\xi')\,\mathrm{d}\xi'\right], \tag{4}$$

where the unknown, streamwise varying wavenumber $\alpha(\xi)$ is determined in the course of the solution by imposing an additional constraint

$$\int_{\eta}\hat{\mathbf{q}}^*\frac{\partial\hat{\mathbf{q}}}{\partial\xi}\,h_\xi\,h_\zeta\,\mathrm{d}\eta\,\mathrm{d}\zeta = 0, \tag{5}$$

and requiring the amplitude functions $\hat{\mathbf{q}}(\xi,\eta,\zeta) = (\hat{\rho},\hat{u},\hat{v},\hat{w},\hat{T})^T$ to vary slowly in the streamwise direction in comparison with the phase term $\exp\left[\mathrm{i}\int_{\xi_0}^{\xi}\alpha(\xi')\,\mathrm{d}\xi'\right]$. Substituting Eq. (4) into the HLNSE and invoking scale separation between the streamwise coordinate and the other two directions to neglect the viscous terms with streamwise derivatives, the PSE are obtained in the form

$$\left(\mathbf{L}_{PSE} + \mathbf{M}_{PSE}\frac{1}{h_\xi}\frac{\partial}{\partial\xi}\right)\hat{\mathbf{q}}(\xi,\eta) = 0. \tag{6}$$

The onset of laminar-turbulent transition is estimated by using the logarithmic amplification ratio, the so-called N-factor, relative to the location ξ_I where the disturbance first becomes unstable,

$$N_\phi = -\int_{\xi_I}^{\xi}\alpha_i(\xi')\,\mathrm{d}\xi' + \ln\left[\hat{\phi}(\xi)/\hat{\phi}(\xi_I)\right]. \tag{7}$$

Here, $\hat{\phi}$ denotes an amplitude norm of $\hat{\mathbf{q}}$ at a given ξ, e.g., wall-pressure disturbance or total disturbance energy E [79, 80].

The evolution of convective boundary-layer instabilities is analyzed with a hybrid methodology comprised of PSE and HLNSE solutions across overlapping streamwise domains. The linear amplification of planar and oblique, first and second Mack mode disturbances along the cone is computed with PSE until just upstream of the cone/flare corner. The HLNSE is used to calculate the development of the instability waves through the remaining length of the geometry. Figures 9–10 show the comparison of the N-factor envelopes based on the total disturbance energy for the wind tunnel and flight configurations, respectively. The planar and oblique waves with different azimuthal wavenumbers are given by the legend. For the wind tunnel configuration, the lower Reynolds number reduces the amplification of the disturbances slightly within the cone. The planar and oblique waves with wavenumber $m \leq 20$ are most influenced by the Reynolds number, and no significant differences in amplification are observed on the flare. Figure 9 also shows planar waves not being amplified along the separation region, while the oblique waves are amplified with higher growth rates and become more amplified than the planar waves. For the flight configuration, the lower Reynolds number reduces the amplification of the disturbances on the cone while in the separation region, no amplification of the disturbances is observed. Similar to the wind tunnel configuration, there is a sharp increase in N-factor past reattachment. Comparing the amplification factors obtained prior to the corner to experimental measurements, the N-factors are not sufficient to lead to transition onset on the cone.

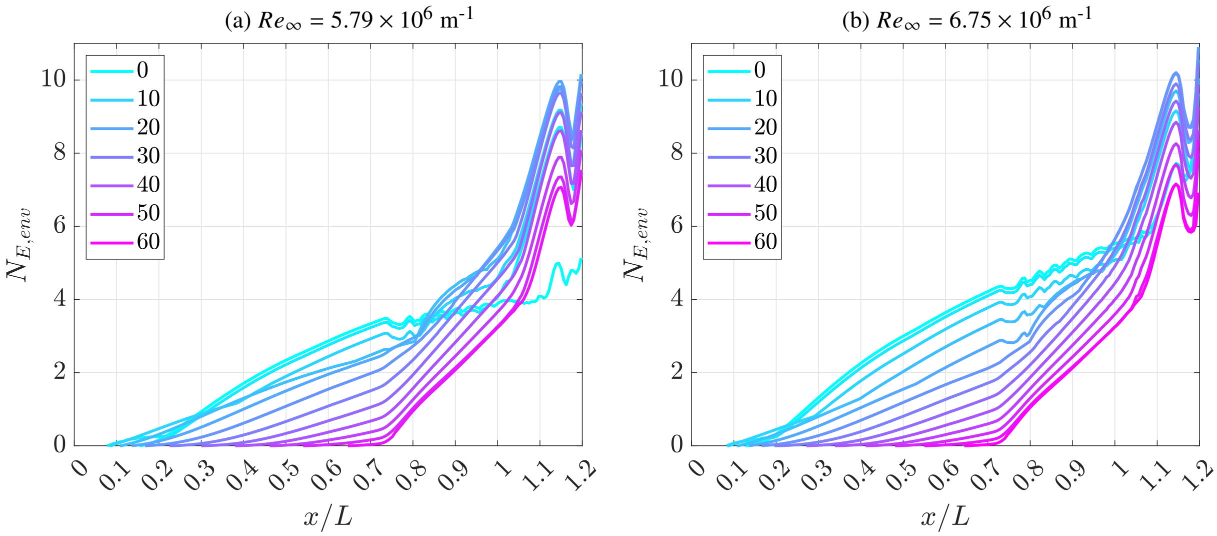

Fig. 9 Evolution of N-factor envelopes based on total disturbance energy ($N_{E,env}$) at the wind tunnel conditions (a) 5.79×10^6 m^{-1} and (b) 6.75×10^6 m^{-1} freestream unit Reynolds numbers. Legend provides azimuthal wavenumber.

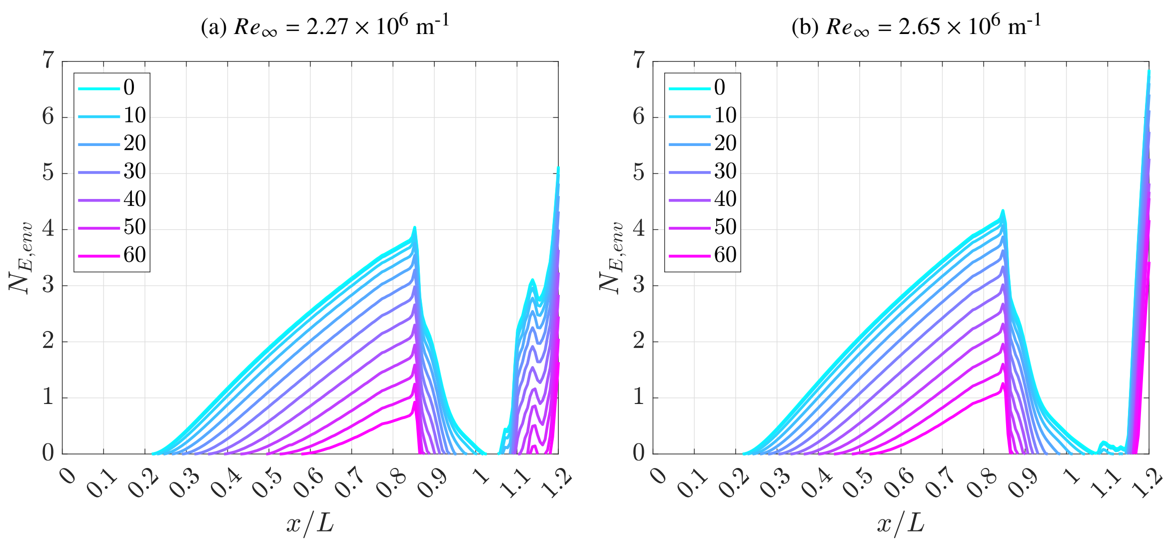

Fig. 10 Evolution of N-factor envelopes based on total disturbance energy ($N_{E,env}$) at the flight conditions (a) 2.27×10^6 m^{-1} and (b) 2.65×10^6 m^{-1} freestream unit Reynolds numbers. Legend provides azimuthal wavenumber.

The global stability analysis (GSA) is based on the HLNSE, with the real-valued angular frequency ω from Eq. (2) replaced by a complex value $\Omega = \omega + i\sigma$, where σ is the temporal growth rate of the disturbance. After setting $\check{\mathbf{f}} = 0$ and defining $\hat{\mathbf{q}} \equiv \check{\mathbf{q}}$, Eq. (3) can be written as the generalized eigenvalue problem,

$$\mathbf{A}\hat{\mathbf{q}} = \Omega \mathbf{B} \hat{\mathbf{q}}, \tag{8}$$

where the leading eigenvalues Ω and eigenvectors $\hat{\mathbf{q}}$ are calculated with the Arnoldi algorithm [81].

A grid sensitivity analysis was performed by Ref. [23] using different grid resolutions for the computation of the laminar basic state. For each grid, the solution was used to compute the azimuthal wavenumber associated with the maximum global instability, and the resulting wavenumbers between the grid used herein (1601×601) and a finer grid (2401×801) were shown to be within 1% relative error.

The leading global instability growth rate at all conditions given in Table 3 is shown in Fig. 11. For all conditions, the flow was globally unstable. The leading unstable mode is a short-wavelength, stationary disturbance with wavenumber slightly increasing as the Reynolds number was increased. For the wind tunnel conditions, the wavenumber increases from m = 48.7683 to m = 50.2553 as Reynolds number is increased from $Re_\infty = 5.79 \times 10^6$ m^{-1} to 6.75×10^6 m^{-1}. For the flight conditions, the wavenumber increases from m = 100.134 to m = 104.829 as the freestream unit Reynolds number is increased from $Re_\infty = 2.27 \times 10^6$ m^{-1} to 2.65×10^6 m^{-1}.

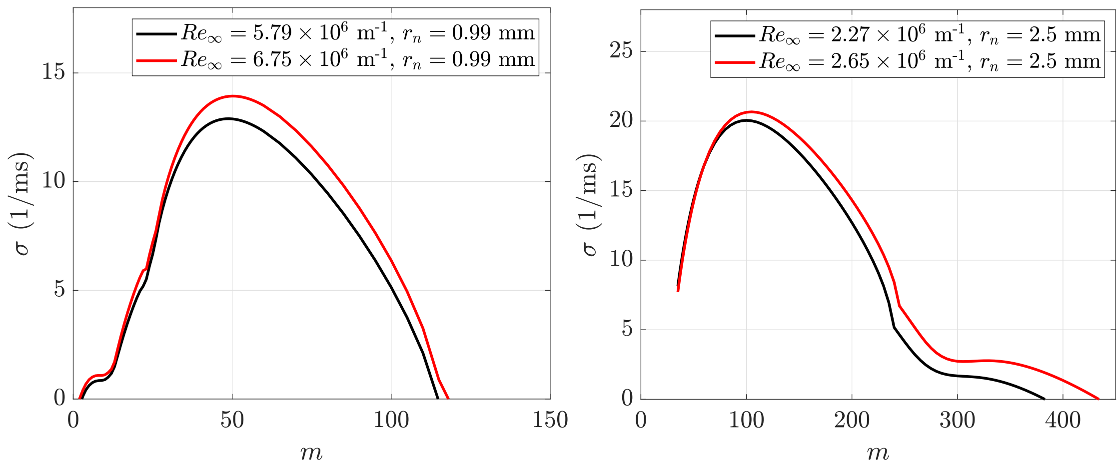

Fig. 11 Leading instability obtained from global instability analysis as function of wavenumber for the (a) wind tunnel and (b) flight conditions.

The real part of the azimuthal velocity component of the corresponding global mode eigenfunctions for the ANDLM6QT and flight conditions at peak growth rates are plotted in Fig. 12. The boundary-layer edge is displayed for each mode shape as a solid black line and is defined more precisely by $h_0/h_{0,\infty} = 0.995$. In addition, the first and second separation regions are shown by dashed black lines at $u = 0$. This short-wavelength mode is concentrated at the reattachment location with no significant presence at the corner. It straddles the separation line of the first, larger, separated region. They are qualitatively identical to the corresponding global mode at wind tunnel and flight conditions matching the AFRL M6LT (not shown).

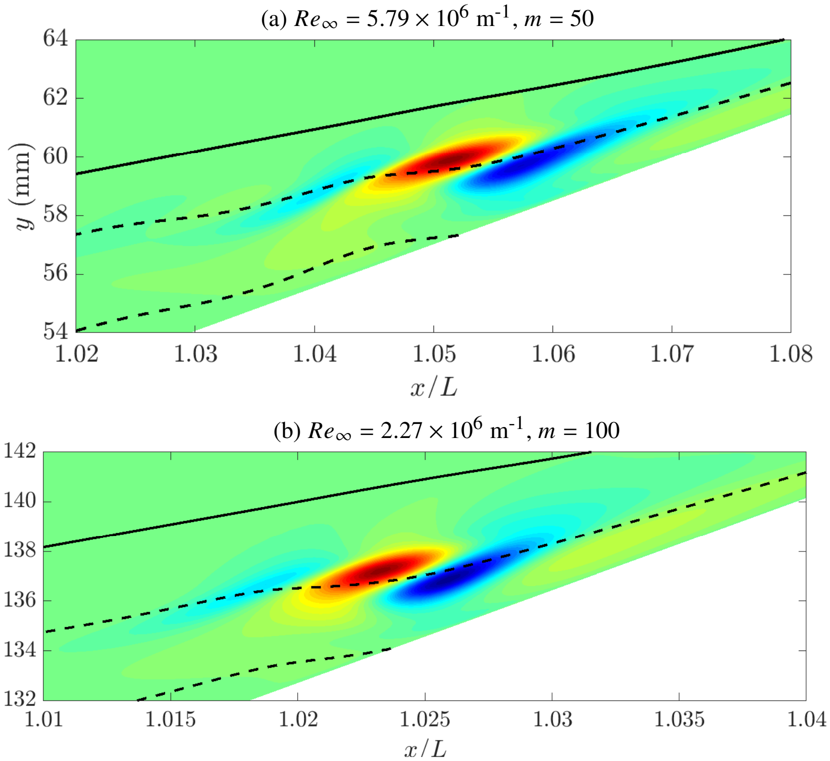

Fig. 12 Real part of streamwise velocity perturbation corresponding to the leading disturbance as computed by global instability analysis for the (a) ANDLM6QT and (b) flight conditions.

VII. Experimental Results

A. Thermography

Figure 13 displays St contours and streamwise profiles for $Re_\infty = 8.4 \times 10^6$ and 12.0×10^6 m^{-1} for the scaled ROTEX-T geometry. Spanwise variation in the contours is minimal, indicating the model is well aligned near zero degrees angle of attack. Alongside the streamwise profiles are empirical correlations for laminar and turbulent heating on a 7° half-angle cone [5]. The close agreement between the laminar correlation and experimental observation suggests that the boundary layer on the conical forebody is laminar prior to the SWBLI. For an incoming laminar boundary-layer, the separation location is determined as the point where $St(x/L)$ exhibits a sudden decrease from its smooth trend ([1, 82]), and are denoted by orange circles in Fig. 13. As Re_∞ increases, the separation point approaches the corner. Within separation, St remains low until the cone/fare junction.

For a laminar boundary layer at separation, zero, one, or two local heating maxima will be observed on the flare, depending on the state of the flow at reattachment.

Zero local maximum indicates either a transitional reattaching boundary layer or the absence of reattachment. This result was observed on ROTEX-T at the lower Reynolds numbers tested (as shown in Fig. 13a). For such cases, determining whether and where reattachment occurs solely from surface heating poses a challenge [1]. As will be described in §VII.B, off-wall measurements were used to determine reattachment for the transitional boundary layer (yellow square in Fig. 13a).

One heating peak occurs on the flare when the reattaching boundary layer is fully laminar, near the end of transition, or turbulent [1, 4, 14]. Reattachment is taken to be the streamwise location of peak St [83], although the actual reattachment point lies slightly upstream of the peak heating location [4].

Two local heating maxima on the flare may also indicate either of two causes. One is transition from laminar to turbulent flow: an initial peak at (laminar) reattachment, a decrease as the boundary layer grows, and eventually a second peak at the end of transition/onset of turbulence [1]. Because of the relatively short flare length compared to the reattachment location at the lowest Re_∞ tested, this case was not observed with the scaled ROTEX-T model. The other flow topology that leads to two heating peaks is a separation location close to (but upstream of) the corner,

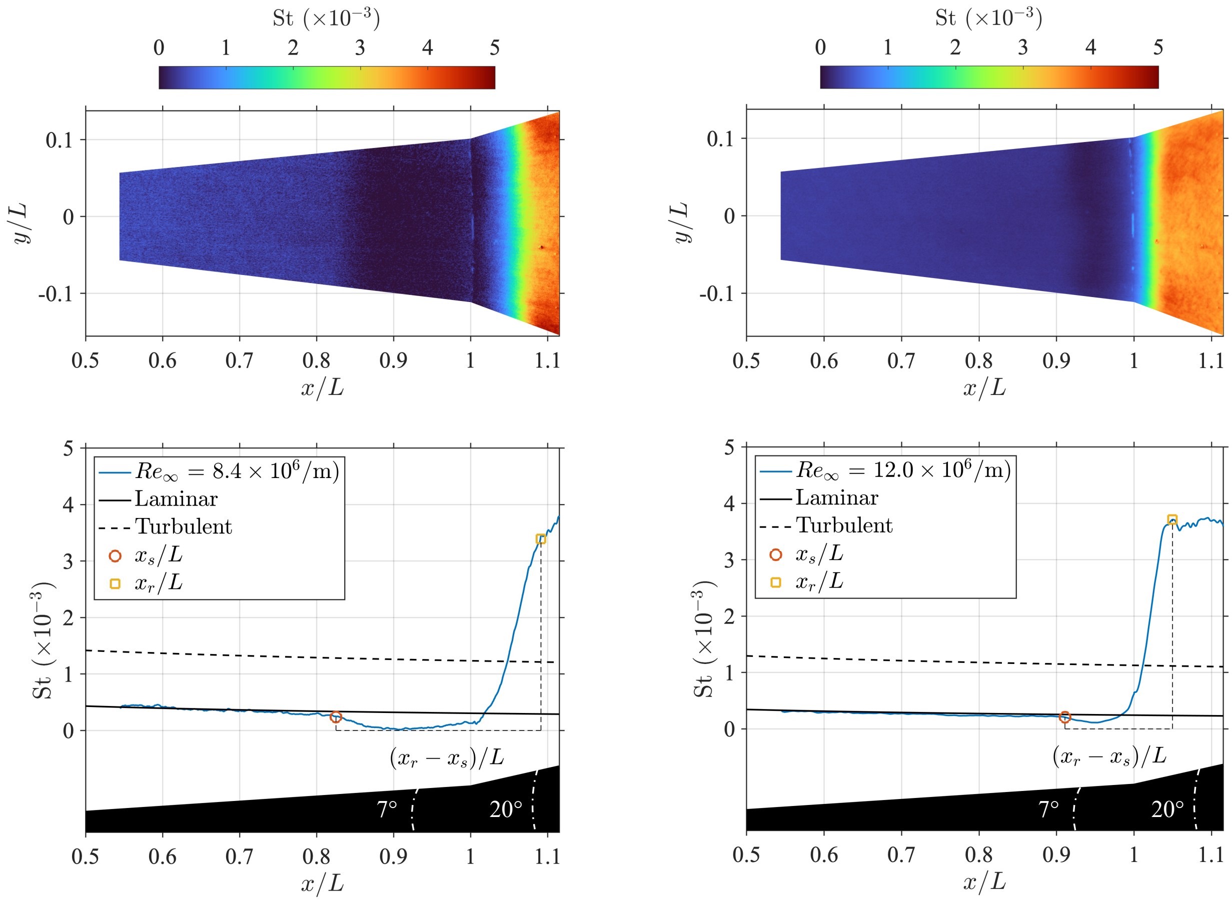

(a) $Re_\infty = 8.4 \times 10^6$ **m**$^{-1}$**.**

(b) $Re_\infty = 12.0 \times 10^6$ **m**$^{-1}$**.**

Fig. 13 Contours and streamwise profiles of St**. Scaled ROTEX-T (**$r_n = 0.99$ **mm),** $M_\infty = 5.7$**.**

such that the separation and reattachment shocks interact [4]. This interaction (an Edney Type VI [6, 84]) generates an expansion wave that impinges on the flare downstream of reattachment, reducing density and heating. This result was observed for this model at the highest Re_∞ for which the boundary layer remained laminar at separation (Fig. 13b).

Evaluating the boundary-layer state at reattachment solely from surface heating at any one condition is impossible because of the potential ambiguity. One peak indicates a fully laminar *or* nearly/fully turbulent boundary layer. Zero peaks indicate a transitional boundary layer *or* no reattachment at all.

Figure 14 shows streamwise profiles of Stanton number for the scaled ROTEX-T for Re_∞ from 5.8×10^6 to 12.0×10^6 m^{-1} at $M_\infty = 5.7$. The profiles on the cone and flare are plotted separately to optimize their scales independently. The black solid and dashed lines are laminar and turbulent St correlations at the minimum and maximum Re_∞. St on the cone agrees well with laminar correlations until a distinct heating 'bucket' upstream of the cone-flare junction, which is a hallmark of laminar separation [1, 83]. For these reasons, it is inferred that the boundary layer is laminar as it approaches the SWBLI. BOS-measured separation and reattachment locations (see §VII.B) are denoted by black circles. The distinct decrement in St is highly correlated with off-wall separation measurements. As Re_∞ increases, the separation location moves downstream. The angular deflection of the flow at separation is essentially insensitive to Re_∞, thus reattachment concomitantly moves upstream, and the separation bubble shrinks. This trend is consistent with previous studies for which the boundary-layer state is laminar prior to the SWBLI and transitional or turbulent upon reattachment [1, 4, 23, 83, 85, 86].

The dependence of separation and reattachment locations on Reynolds number helps determine the state of the reattaching flow. Separation moving upstream as Re_∞ increases indicates a fully laminar shear layer and reattaching

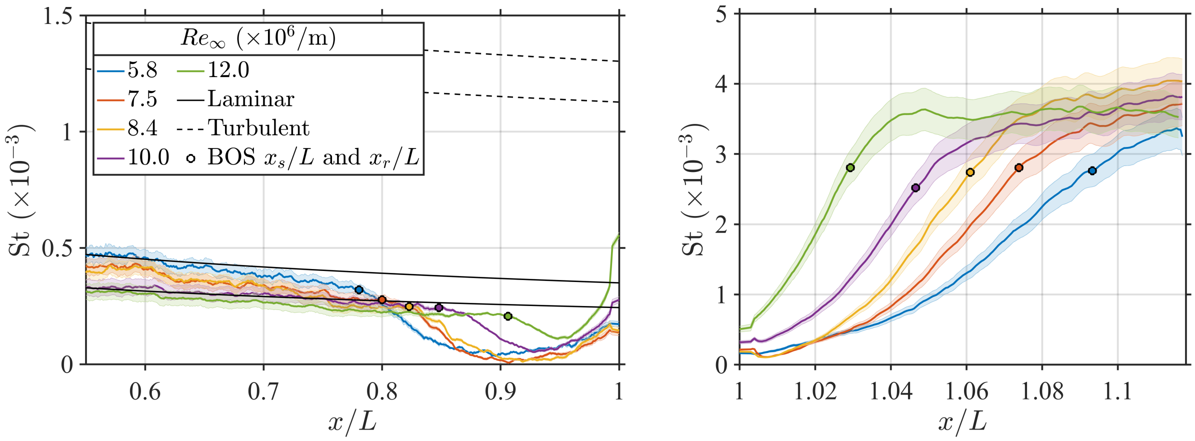

(a) Cone. **(b) Flare.**

Fig. 14 Effect of Re_∞. Scaled ROTEX-T (r_n = 0.99 mm), M_∞ = 5.7 ANDLM6QT.

boundary layer [85, 87]. A reversal occurs for sufficiently high Re_∞ such that the shear layer becomes transitional, and separation hence moves downstream as Re_∞ increases [85]. The monotonic increase of separation location with Reynolds number proves that the reattaching flow is at least transitional, and maybe turbulent, but not laminar.

For Re_∞ of 10.0×10^6 m^{-1} and less, St increases continuously up to the end of the flare (Fig. 14b), rendering it ambiguous whether and where reattachment occurs. However, off-wall measurements show shear-layer reattachment, indicating the flow is transitional. A local St maximum is observed at $x/L \approx 1.04$ for $Re_\infty = 12.0 \times 10^6$ m^{-1} suggesting the flow has reached the end of transition at reattachment. Off-wall measurements indicate reattachment upstream of the peak heating, at $x/L = 1.03$.

Figure 15 shows heating profiles on the baseline geometry obtained in the AFRL M6LT, for which the freestream Mach number is 6.14. Note that the infrared camera field of view extended farther upstream for tests in this facility, thus the profiles begin closer to the nose. For $Re_\infty = 2.2 \times 10^6$ to 6.8×10^6 m^{-1}, laminar separation and transitional reattachment were observed. For $Re_\infty = 9.0 \times 10^6$ m^{-1} and higher, heating rises upstream of the cone flare junction, indicating a transitional boundary layer entering the SWBLI. This differs from tests in the ANDLM6QT (with its lower Mach number and different noise environment), for which the forebody boundary layer remained laminar at higher Re_∞ [88, 89]. The flow was transitional at reattachment for $Re_\infty \leq 6.8$ and turbulent for higher Re_∞.

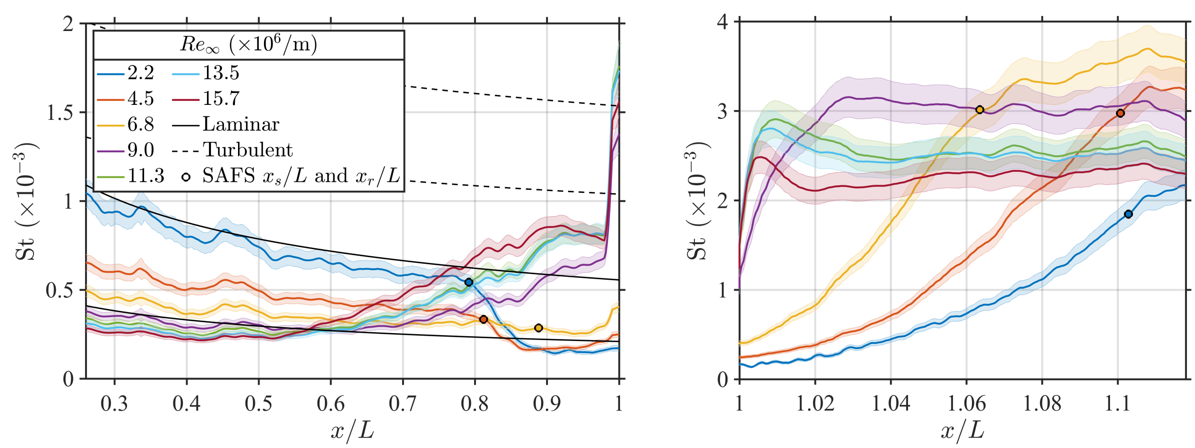

(a) Cone. **(b) Flare.**

Fig. 15 Effect of Re_∞. Scaled ROTEX-T (r_n = 0.99 mm), M_∞ = 6.14 AFRL M6LT.

Nose radius affected the SWBLI through the modulated flow on the conical forebody. Figure 16 shows $St(x/L)$ for the highest Re_∞ tested in the ANDLM6QT, 12.0×10^6 m^{-1}. Flow separated earlier for the 5 mm radius nose, thus delaying reattachment. The heating distribution and off-wall measurements indicate transitional flow at reattachment, as for the baseline nose radius. For the sharp nose, St rises upstream of the cone-flare junction, and since it is below the turbulent correlation, the boundary layer is surmised to be transitional prior to the SWBLI. Stability analysis indicates the N-factor is greater than 8 at the cone-flare junction for $Re_\infty = 12.1 \times 10^6$ m^{-1} (see Fig. 4e in Ref. [23]), which for conventional-noise facilities usually correlates with transitional flow [26]. The surface indication of separation for a transitional boundary layer has previously been shown to correlate with a slight plateau in St prior to its abrupt increase [23]. This signature occurred at $x/L = 0.98$, and it correlates well with the off-wall measurement. A distinct heating peak at reattachment indicates the flow is at the end of transition [90]. At the lower Re_∞ tested, laminar separation and transitional reattachment were observed for the sharp nose.

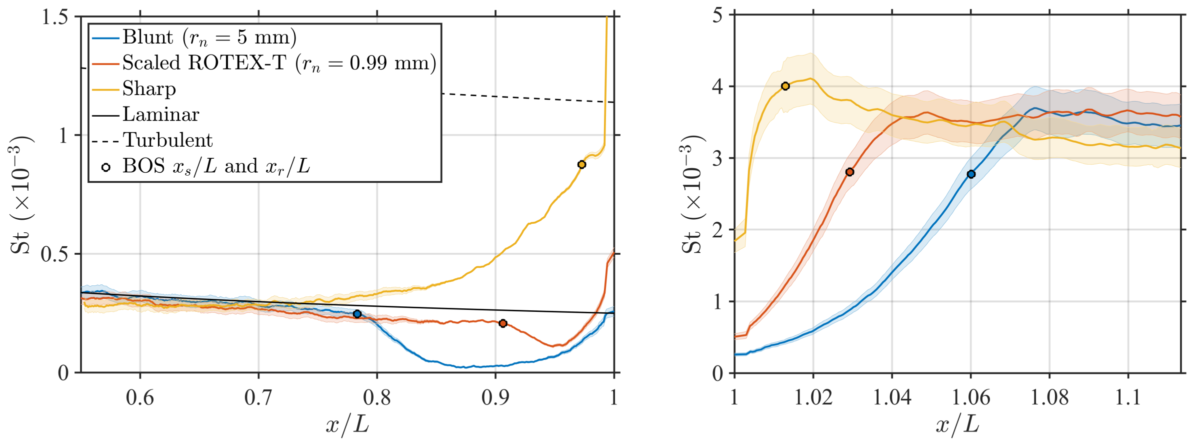

(a) Cone. **(b) Flare.**

Fig. 16 Effect of nose radius. $Re_\infty = 12.0 \times 10^6$ **m^{-1} (note that** $Re_\infty = 12.2 \times 10^6$ **m^{-1} was used for** $r_n = 5$ **mm),** $M_\infty = 5.7$**.**

For the range of Re_∞ tested in the AFRL M6LT (2.2×10^6 to 24.7×10^6 m^{-1}), transition on the cone did not occur for the blunt nose tip, but it did for the scaled ROTEX-T (at $Re_\infty = 9.0 \times 10^6$ m^{-1}) and sharp noses (at $Re_\infty = 6.8 \times 10^6$ m^{-1}). For the 5 mm radius nose, the shear layer did not reattach at the lowest Re_∞ of 2.2×10^6 m^{-1}, as indicated by SAFS measurements. As Re_∞ increased, separation shifted upstream until reattachment occurred at $Re_\infty = 9.0 \times 10^6$ m^{-1}. With further increases in Re_∞, separation moved downstream.

B. High-Resolution Background-Oriented Schlieren

Figure 17 displays density contours of the scaled ROTEX-T configuration for $Re_\infty = 5.8 \times 10^6$ to 12.0×10^6 m^{-1}. The density has been normalized by the freestream density. The bow shock is visible entering the field of view at $y/L = 0.17$, and downstream of it, ρ/ρ_∞ exceeds unity. The separation shock is marked by a sudden streamwise increase in density in proximity to the model surface ($\rho/\rho_\infty \approx 2.0$). The reattachment shock forms near the flare surface, where density peaks ($\rho/\rho_\infty \approx 3.0$). The low-density recirculation bubble is situated between the separation and reattachment locations. As Re_∞ increases, the boundary layer on the conical forebody thins, and the shear layer approaches the surface. Moreover, the separation point moves downstream as Re_∞ increases. The angle between the surface and shear layer does not vary with Re_∞, thus the reattachment point moves upstream, and the recirculation bubble diminishes in size, trends consistent with the IR results.

A slightly negative streamwise density gradient is observed between the separation and reattachment shocks. This is because the separation shock redirects the flow away from the wall, while the dividing streamline curves toward it, causing flow expansion. The axisymmetric geometry further amplifies this through a three-dimensional relieving effect. For most Reynolds numbers tested, density downstream of the reattachment shock increases as Re_∞ increases. However, this trend ceases for $Re_\infty = 12.0 \times 10^6$ m^{-1}, because the separation and reattachment shocks intersect near the surface. An expansion fan emanates from this point, resulting in lower density downstream of reattachment and the local heating minimum observed by the IR thermography.

Figure 18 presents normalized density profiles at various streamwise positions as functions of the polar angle θ. The Taylor–Maccoll inviscid solution, which is not valid in the boundary layer or separated region, is shown for

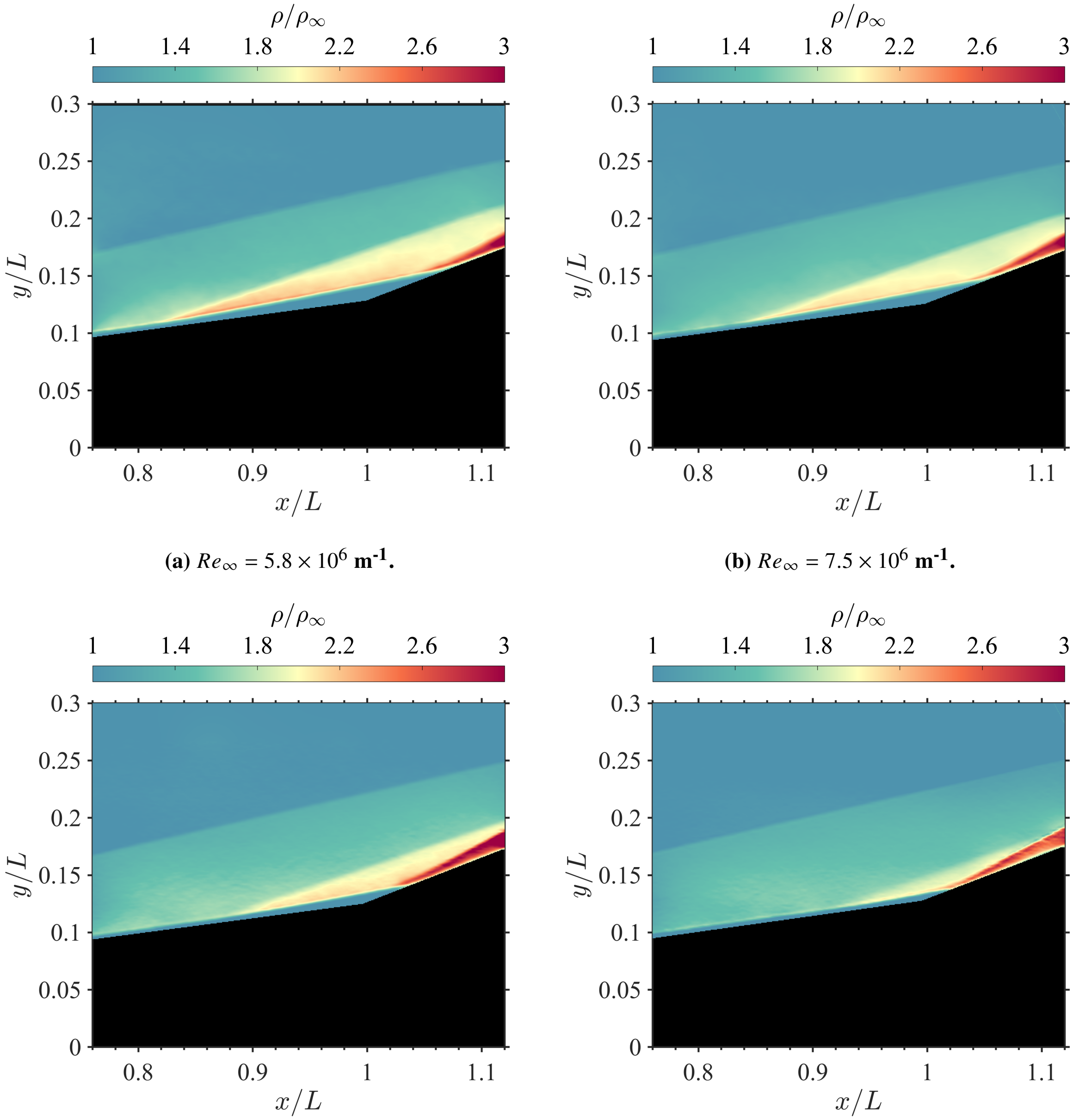

(a) $Re_\infty = 5.8 \times 10^6$ **m^{-1}.**

(b) $Re_\infty = 7.5 \times 10^6$ **m^{-1}.**

(c) $Re_\infty = 10.0 \times 10^6$ **m^{-1}.**

(d) $Re_\infty = 12.0 \times 10^6$ **m^{-1}.**

Fig. 17 Normalized density fields from high-resolution BOS. Scaled ROTEX-T ($r_n = 0.99$ mm).

comparison [9]. The BOS-measured density is nearly constant outside the bow shock (i.e., $\theta \gtrsim 12.5°$), where uniform freestream conditions are expected (i.e., $\rho/\rho_\infty = 1$). Excellent agreement is observed between the inviscid solution and the BOS-measured density outside the separation bubble.

Density profiles along the flare are illustrated in Fig. 19. The minimum polar angle ($\theta = 20°$) corresponds to the surface of the flare. Reattachment is marked by near-wall density exceeding the density behind the separation shock.

Profiles of the wall-normal distance at which $\partial\rho/\partial y$ peaks (δ) are presented in Fig. 20. This is a convenient definition for the boundary-layer edge (for attached flow) and shear-layer location (for separated flow) from BOS measurements. (The separation bubble edge — the zero-velocity streamline dividing forward and reversed flow — is slightly closer to the wall than the shear layer.) The boundary layer thickness δ/L is initially nearly constant prior to separation, whereupon it increases. The slope of the shear-layer edge decreases slightly as Re_∞ increases. As Re_∞

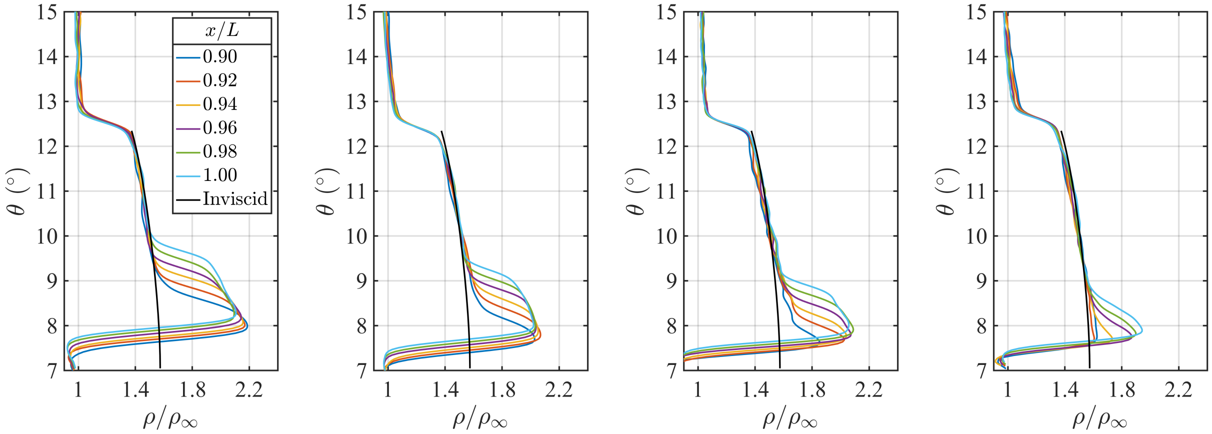

(a) $Re_\infty = 5.8 \times 10^6$ **m^{-1}.** **(b)** $Re_\infty = 7.6 \times 10^6$ **m^{-1}.** **(c)** $Re_\infty = 10.0 \times 10^6$ **m^{-1}.** **(d)** $Re_\infty = 12.0 \times 10^6$ **m^{-1}.**

Fig. 18 Normalized density profiles, ρ/ρ_∞, on the conical forebody. Scaled ROTEX-T (r_n = 0.99 mm).

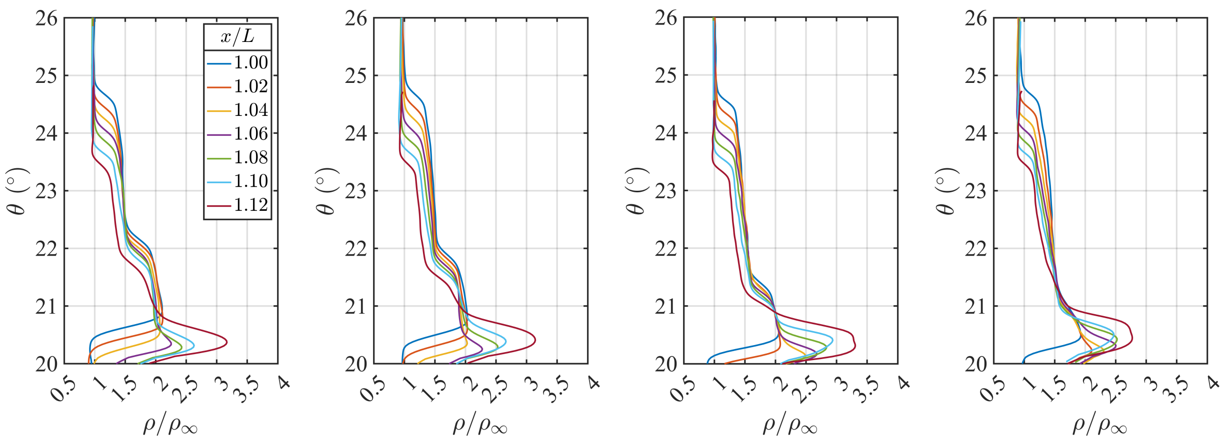

(a) $Re_\infty = 5.8 \times 10^6$ **m^{-1}.** **(b)** $Re_\infty = 7.6 \times 10^6$ **m^{-1}.** **(c)** $Re_\infty = 10.0 \times 10^6$ **m^{-1}.** **(d)** $Re_\infty = 12.0 \times 10^6$ **m^{-1}.**

Fig. 19 ρ/ρ_∞ profiles on the flare. Scaled ROTEX-T (r_n = 0.99 mm).

increases, the edge thickness at reattachment decreases.

Surface and off-wall measurements are overlaid in Fig. 21. Contours of *St* are displayed along with BOS-measured density fields (above) and the density gradient magnitude (below). The correspondence between the separation shock origin and decreasing surface heating is striking. The decrease in separation bubble size with increasing *Re* is consistent with previous experiments studying transitional SWBLIs for flare half-angles ranging from 17.5–43° [1, 3, 4, 15, 21, 85, 87]. As observed previously, the reattachment location precedes peak heating [4].

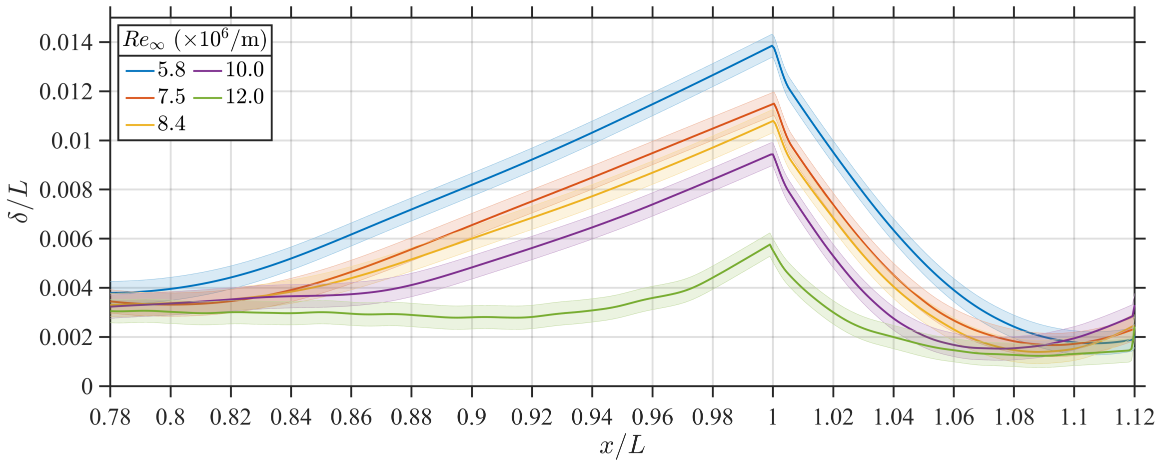

Fig. 20 Location of maximum $\partial\rho/\partial y$. Scaled ROTEX-T (r_n = 0.99 mm).

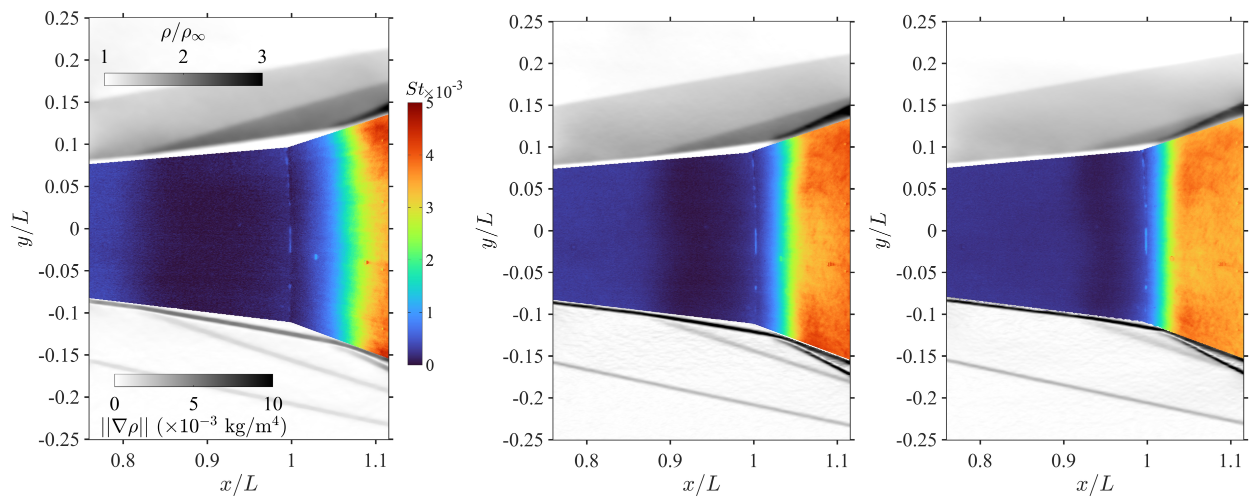

(a) $Re_\infty = 5.8 \times 10^6$ **m^{-1}.** **(b)** $Re_\infty = 10.0 \times 10^6$ **m^{-1}.** **(c)** $Re_\infty = 12.0 \times 10^6$ **m^{-1}.**

Fig. 21 Off-wall and surface measurement comparison, scaled ROTEX-T (r_n = 0.99 mm).

C. High-Speed Self-Aligned Focusing Schlieren

High-speed self-aligned focusing schlieren (SAFS) was used in the AFRL M6LT to study the general separation bubble trends and disturbance shapes by conducting an spectral proper-orthogonal decomposition (SPOD) analysis. Time-averaged background-subtracted SAFS images, overlaid with *St* contours, are presented in Fig. 22. The *St* contours are calculated as a temporal average over 10 frames (0.014 s), whereas the SAFS images are averaged over 110 frames (0.007 s), both during the M6LT's second period of steady flow. The SAFS images are on a plane through the model axis. For conditions where a separation bubble is clearly visible, the separation shock and shear layer are emphasized with blue and yellow linear fits. Since the shear layer curves downstream of the cone/flare junction, its fit is based on two points upstream of the junction. Separation was determined as the intersection of the linear fits for the separation shock and shear layer and is marked with a red "×." Reattachment was assessed as the point where the linear fit of the shear layer intersects the flare. The separation and reattachment locations determined from SAFS are consistent with those determined from the *St* distributions.

In the instantaneous, mean-subtracted SAFS images, density fluctuations were observed between the shear layer and

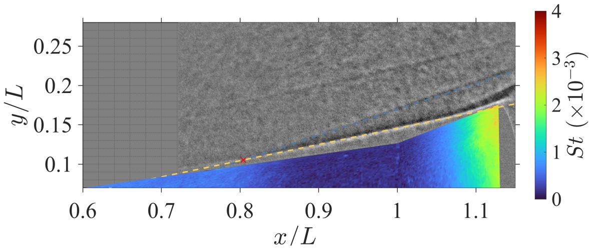

(a) Re_∞ **= 2.2 × 10^6 m^{-1}.**

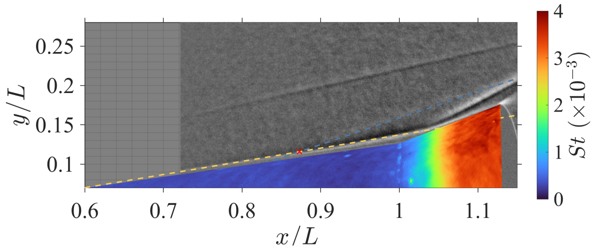

(b) Re_∞ **= 6.8 × 10^6 m^{-1}.**

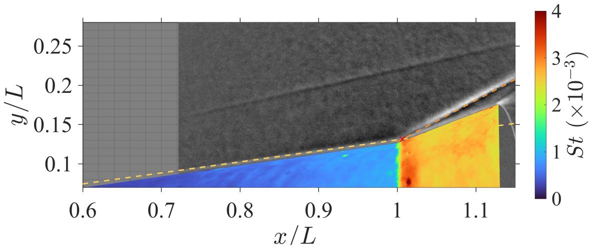

(c) Re_∞ **= 11.3 × 10^6 m^{-1}.**

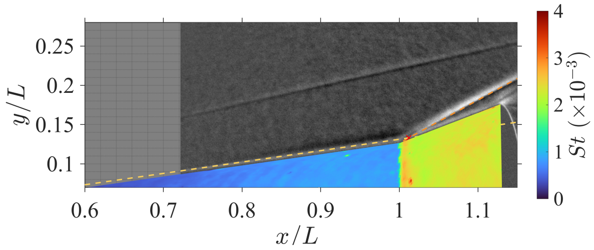

(d) Re_∞ **= 15.7 × 10^6 m^{-1}.**

Fig. 22 SAFS and St**. Scaled ROTEX-T (**r_n **= 0.99 mm),** M_∞ **= 6.14.**

the separation shock (Fig. 23). These fluctuations were strongest for the 5 mm radius nose, and still discernible for the scaled ROTEX-T nose, but not present with the sharp nose. These waves have not been observed previously with similar geometries (such as a cone-cylinder-flare, which has an expansion corner upstream of the compression corner), even with blunter nosetips.

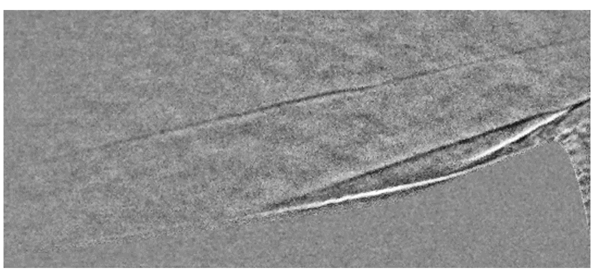

(a) Sharp nose, Re_∞ **= 4.6 × 10^6 m^{-1}.**

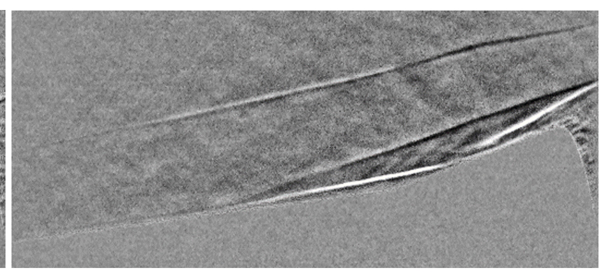

(b) r_n **= 0.99 mm,** Re_∞ **= 6.8 × 10^6 m^{-1}.**

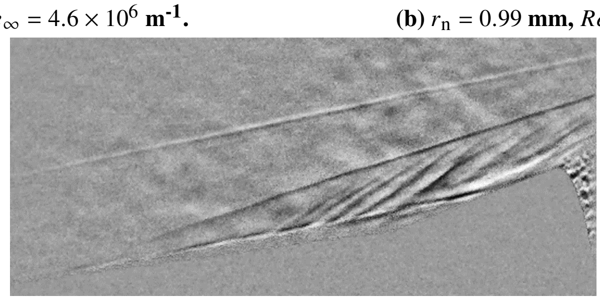

(c) r_n **= 5 mm,** Re_∞ **= 13.5 × 10^6 m^{-1}.**

Fig. 23 Instantaneous SAFS images.

To get a better understanding of the frequencies and disturbance shapes present, a SPOD analysis was conducted. For the scaled ROTEX-T nose, no flow-related frequency peaks were observable in the mode energy for $Re_\infty = 6.7 \times 10^6$ m^{-1} (Fig. 24a). However, decreasing the freestream unit Reynolds number to 4.6×10^6 m^{-1} revealed several peaks. Although those above 100 kHz did not correspond to flow features, the peak at 36 kHz appears to be a shear-layer instability (Fig. 24c).

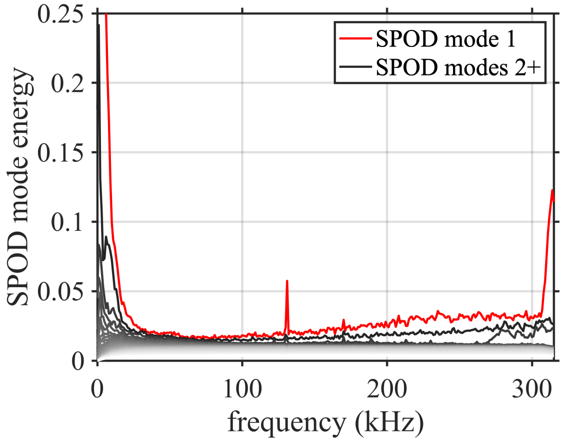

(a) Relative mode energy, $Re_\infty = 6.7 \times 10^6$ **m^{-1}.**

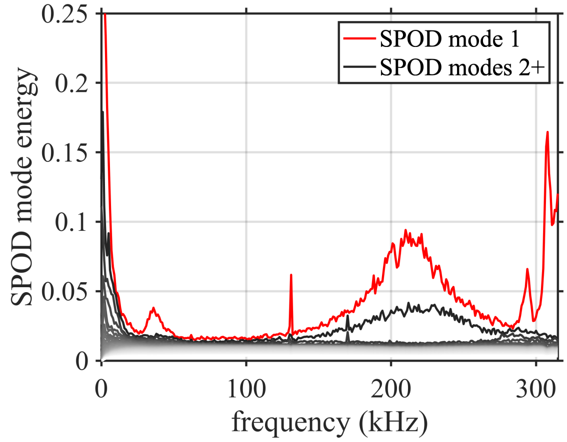

(b) Relative mode energy, $Re_\infty = 4.6 \times 10^6$ **m^{-1}.**

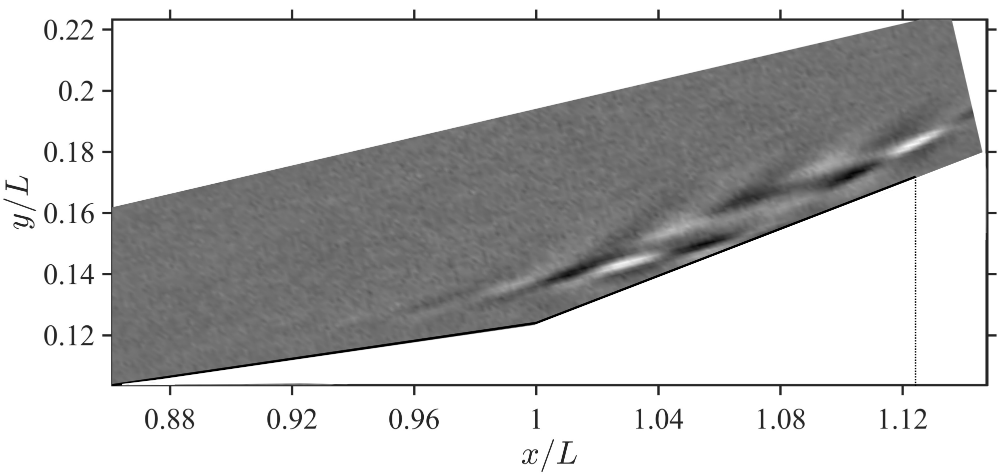

(c) Mode shape, $f = 36$ **kHz,** $Re_\infty = 4.6 \times 10^6$ **m^{-1}.**

Fig. 24 SPOD mode energy and shape, scaled ROTEX ($r_n = 0.99$)**.**

D. Linear Array Focused-Laser Differential Interferometry

Linear array focused-laser differential interferometry (LA-FLDI) was used to measure the spectral content in the separation shock layer. Due to the large number of runs necessary to obtain the full vertical traversal, only one freestream unit Reynolds number was investigated for each nose radius. Figure 25 shows a contour plot of the concatenated LA-FLDI results for the scaled ROTEX-T nosetip. A peak at around 52 kHz exists about 4.8 mm off the surface. It is at a slightly higher frequency than the SPOD peak, and likely represents the shear-layer mode. LA-FLDI detected a second peak at around 188 kHz, centered 2.8 mm above the surface. This peak corresponds to the Mack's second mode disturbances predicted by linear modal analysis of Fig. 9.

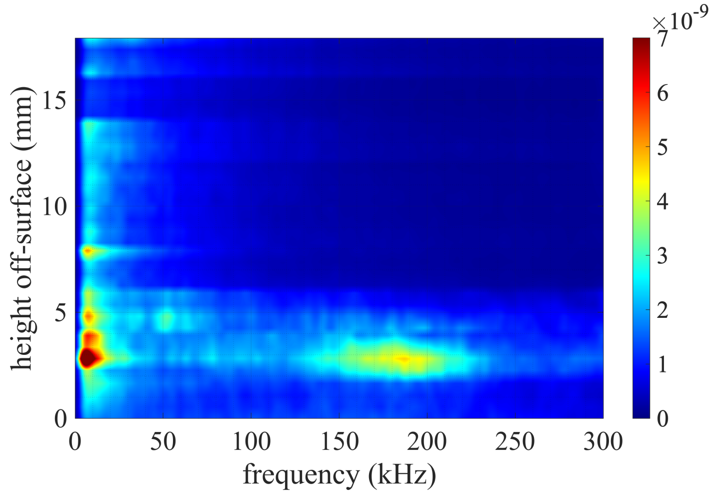

Fig. 25 LA-FLDI power spectral density. Scaled ROTEX-T (0.99 mm), $Re_\infty = 6.8 \times 10^6$ **m**$^{-1}$**.**

VIII. Comparison of Flight-Test, Ground-Test, and Computational Results

A. Density

Figure 26 compares the BOS-measured density field and laminar base flows computed from SU2 and VULCAN-CFD at the primary experimental conditions ($M_\infty = 5.7$, $Re_\infty = 5.8 \times 10^6$ m^{-1}). VULCAN predicts separation at $x/L = 0.72$, slightly upstream of the SU2 prediction (0.74); both are farther upstream than the experimental results ($x_s/L = 0.78$). VULCAN-CFD and SU2 predict reattachment at $x_r/L = 1.118$ and 1.140, while the experimental result was 1.09. The angle of the shear layer relative to the model axis is essentially identical among the three. The subtle negative streamwise density gradient seen in the BOS results (§VII.B) is also replicated in the computations, but it is less pronounced.

The density field computed for flight conditions ($M_\infty = 4.68$, $Re_\infty = 2.3 \times 10^6$ m^{-1}) exhibits later separation, $x_s/L = 0.83$ (Fig. 26b). Lower M_∞ results in both a thinner boundary layer and subsonic region within it, leading to higher velocity near the wall and delayed separation [6]. The departure of the shear layer from the surface is shallower, so the separation shock angle is smaller, yielding lower density in the separation shock layer. Between the later separation and smaller separation shock angle, the reattachment location computed for flight conditions is much earlier ($x_r/L = 1.070$)

Measured and computed density profiles upstream of the cone-flare junction are shown in Fig. 27. The Taylor–Maccoll inviscid solution provides a common reference. The SU2 and VULCAN results match one another closely. Excellent agreement with experiment is observed in the freestream and within the bow shock layer. The bow shock location matches, but the sharp density gradient through the shock is not resolved by the BOS due to the integration when solving the Poisson equation and inability of the Filtered Back Projection Technique to perfectly reconstruct a planar slice of the three-dimensional density field. The computed height above the wall of peak density, including its streamwise variation, also matches the experiment excellently. Inside the separation shock layer, computations show a more uniform density than experiments. Furthermore, the peak density exhibits less streamwise variation.

Density profiles off the flare are shown in Fig. 28. SU2 predicts the bow and separation shocks are slightly closer to the wall than VULCAN-CFD does. Compared to the experiments, the computations show more uniform densities in both the bow and separation shock layers. The inability of the BOS to replicate the sharp density gradient of the bow and separation shocks is again apparent. The density gradient of the reattachment shock, however, is more similar to the computational result. The computations overpredict the peak density behind the reattachment shock by about 15%, and locate the peak density closer to the wall. The net result is a much steeper density gradient at the wall in computations than experiments. It is unclear to what extent this difference arises from the challenge of reconstructing sharp density gradients from BOS, compounded by the difficulty of making BOS measurements very close to the wall.

Differences in the density profiles close to the wall, both in the separation region and after reattachment, can also be partially attributed to the use of a steady-state algorithm to solve this flow field (§VI). This is known to violate topological arguments [64–66, 91], which assert that unsteady two-dimensional laminar separation bubbles are structurally unstable and susceptible to global instability [92, 93]. The size and properties of inherently unsteady phenomena (i.e., the

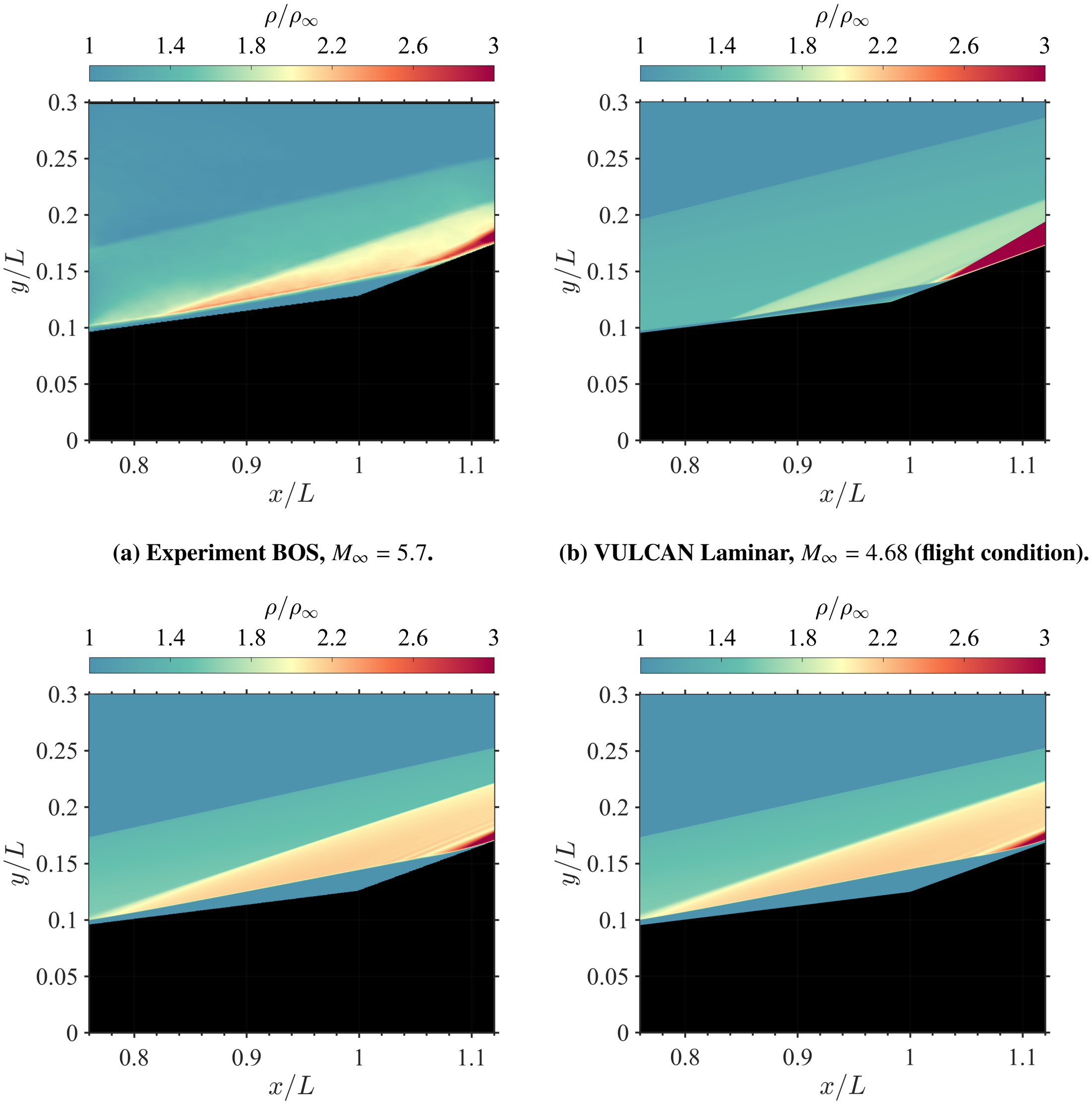

(a) Experiment BOS, $M_\infty = 5.7$.

(b) VULCAN Laminar, $M_\infty = 4.68$ (flight condition).

(c) SU2 Laminar, $M_\infty = 5.7$.

(d) VULCAN Laminar, $M_\infty = 5.7$.

Fig. 26 Normalized density fields, $Re_L = 2.4 \times 10^6$.

separation bubble and reattachment), will be incorrect due to this nonphysical simplification. This cause may also be a factor in the differences between experiment and computation noted in the shock layer near the edge of the separation bubble noted above.

The normalized wall-normal distance to maximum $\partial\rho/\partial y$ is shown in Figure 29. Recall that this definition was used to identify the locations of the boundary-layer edge and shear layer from BOS data. Often in computations, the boundary-layer thickness is identified as somewhere between the wall-normal position to $h_0/h_{0,\infty} = 0.99$ and maximum stagnation enthalpy; this definition of δ is also included for comparison. These criteria were found to match closely, a heretofore unnoticed alignment. This is useful because of the relative ease of experimentally measuring density gradients compared to stagnation enthalpy. The shear-layer height calculated by VULCAN-CFD and SU2 is greater than the experimental result because of the early separation in the simulations. However, the angle of the shear layer relative to the surface, both upstream and downstream of the cone/flare junction, are similar. Note that the above caveat about the limited trustworthiness of a steady, axisymmetric simulation for a laminar separation bubble, applies here as well.

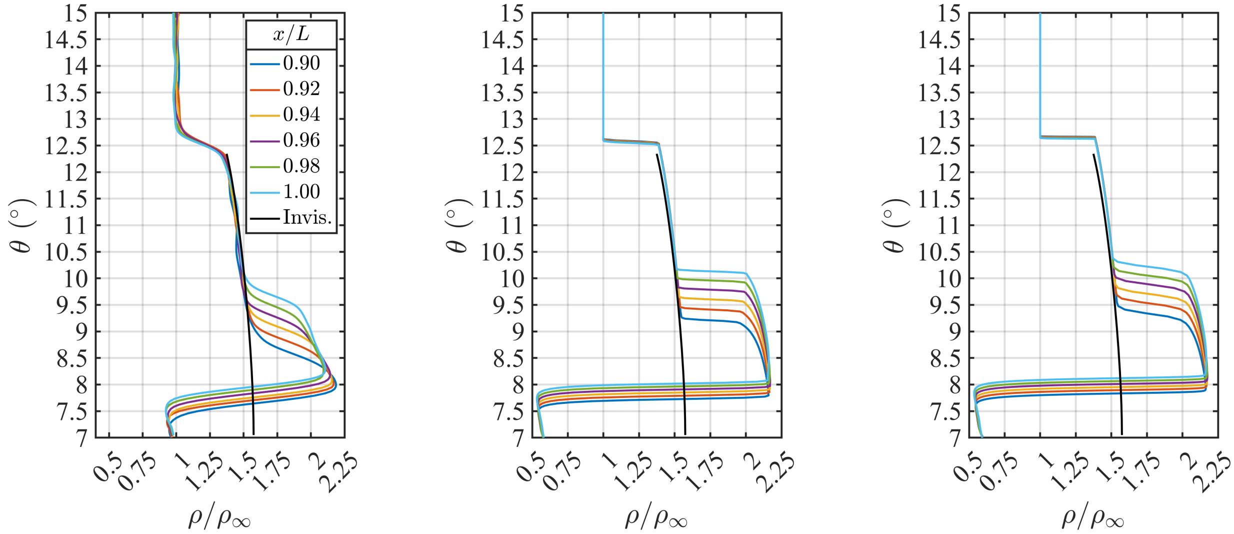

(a) BOS. **(b) SU2 Laminar.** **(c) VULCAN-CFD Laminar.**

Fig. 27 Conical forebody density profiles, $Re_\infty = 5.8 \times 10^6$ m^{-1} and $M_\infty = 5.7$.

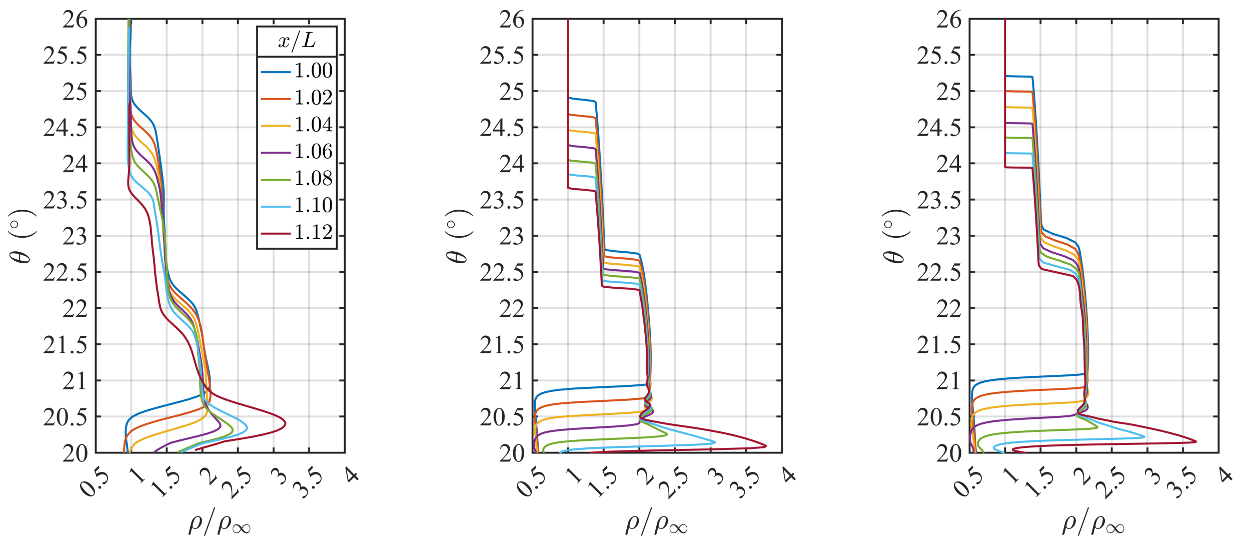

(a) BOS. **(b) SU2 Laminar.** **(c) VULCAN-CFD Laminar.**

Fig. 28 Flare density profiles, $Re_\infty = 5.8 \times 10^6$ m^{-1} and $M_\infty = 5.7$.

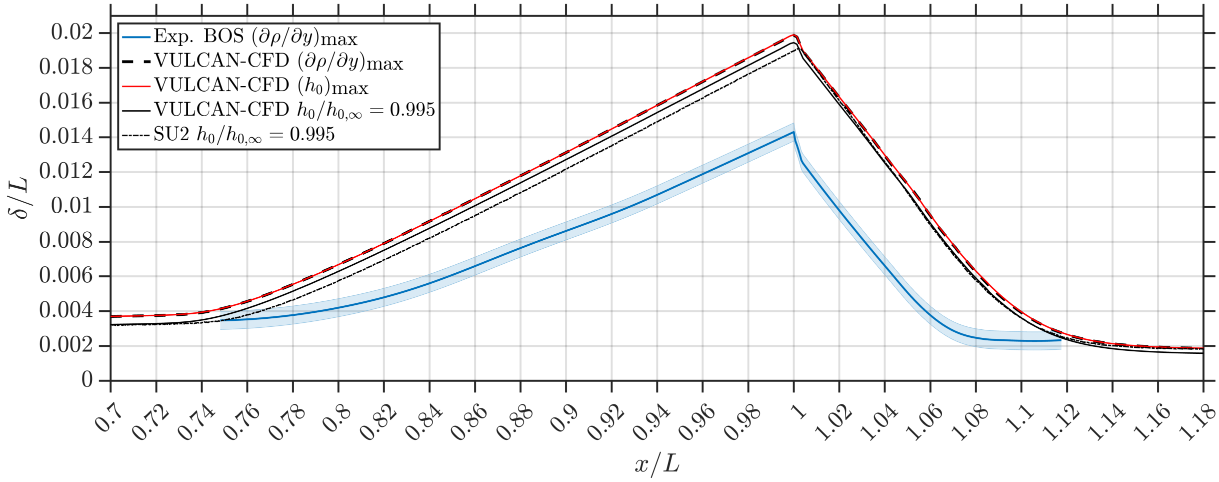

Fig. 29 Boundary-layer thickness and shear-layer location.

B. Temperature and Heating

Figure 30a shows in-flight surface temperature measured by thermocouples (TCs). Figure 30b shows the heat flux calculated from those thermocouple data and measured directly by heat-flux microsensors (HFMs). The time at which flight data was sampled was chosen to match Re_L of the primary ANDLM6QT conditions. Thermocouples TC1, TC2, TC4, TC6, TC7, TC8, and TC9 were used, which are all along the $\phi = 90°$ ray. Heat-flux microsensors HFM9, HFM10, HFM4, HFM11, HFM5, HFM6, and HFM7 were used. To increase the spatial resolution of the profiles, sensors along both the $\phi = 90°$ and 270° rays were incorporated (Fig. 3). To ameliorate the effect of varying α and β, a moving average of heat flux was calculated over 1.05 s, the period of the vehicle axial rotation.

Heat flux calculated from the thermocouples exceeds that measured directly by ≈ 25 kW/m^2 regardless of magnitude, a discrepancy addressed in Ref. [31]. On the one hand, because the materials of a TC and HFM are different, the local heating might be too. But on the other hand, the positive heat flux at the apogee measured by the thermocouples is not plausible, and the measured surface temperatures of HFM and TC sensors do not differ dramatically. Further analysis revealed that possible uncertainties in the material properties, sensor lengths, or absolute temperature measurement at the reference junction can't explain the observed differences. The best agreement between HFM and TC results is if an adiabatic back-face boundary condition is assumed for the TCs. The significant differences between the back-face temperatures calculated with this assumption and those measured indicate insufficient thermal contact or delayed measurement there. Due to the uncertainties in the heat fluxes derived from the thermocouple measurements, their results are not considered in the further analysis.

VULCAN-CFD laminar and turbulent RANS computations at flight conditions (except for a uniform $T_w = 330$ K) are plotted alongside in Fig. 30b. Figure 31 shows analogous plots for the primary AFRL M6LT condition. The temperature and heat-flux distributions are similar, but slightly higher for larger Re_L. Upstream of separation, the measured heat flux closely matches the laminar computation, suggesting that the forebody boundary layer is laminar. In-flight heating at $x/L = 0.87$ is slightly lower than at 0.79, within the measurement uncertainty; a larger decrease in heating exists between 0.87 and 0.95. With the coarse spatial resolution and uncertainty of the flight data, the laminar separation location can't be determined precisely. The VULCAN-CFD computation predicts separation within this range, at $x/L = 0.85$. The computed heat flux in the unambiguously separated region, at $x/L = 0.95$, matches the flight data very closely.

The continuous rise in flight-measured heat flux on the flare suggests that the flow there either is transitional or has not reattached. Considering the separation location is fairly close to the corner ($0.79 < x_s/L < 0.95$), reattachment of a transitional boundary layer is the suspected scenario. References [1, 94] indicate that the ratio of heating at the reattachment point to the minimum heating in the separated region heating is approximately 2 to 3 times higher for a transitional flow at reattachment than a laminar one. That this ratio was around three times larger in flight than in the laminar simulation further supports the conclusion that the flow was transitional at reattachment in flight. In-flight peak heating is approximately three times larger than the laminar computation and slightly above the turbulent

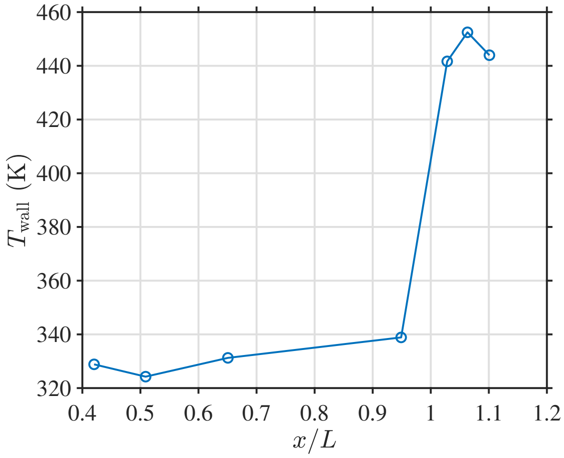

(a) Surface temperature.

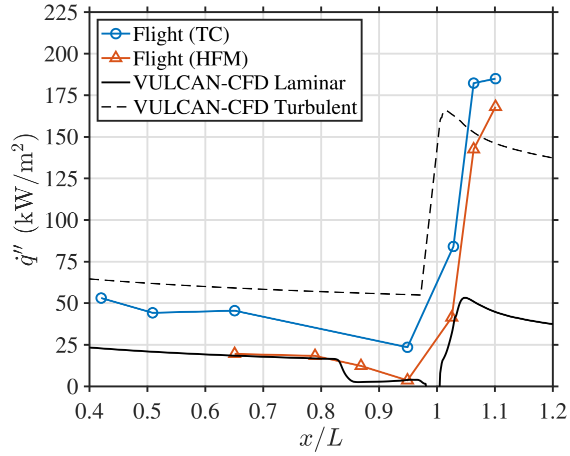

(b) Heat flux.

Fig. 30 Flight temperature and heating. $Re_L = 2.4 \times 10^6$, $M_\infty = 4.68$.

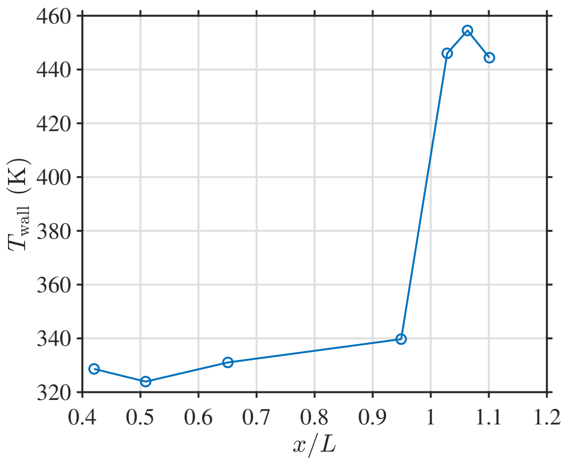

(a) Surface temperature.

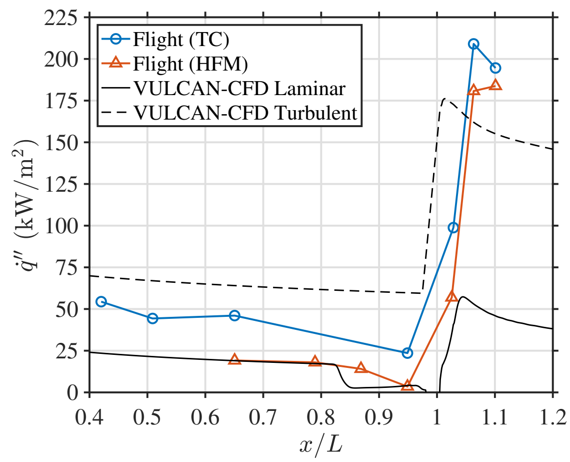

(b) Heat flux.

Fig. 31 Flight temperature and heating. $Re_L = 2.8 \times 10^6$, $M_\infty = 4.61$.

one. As discussed in conjunction with Fig. 14b, a transitional reattachment location cannot be discerned solely from surface heating data, even with much higher spatial resolution than the flight-test instrumentation. Thus, the in-flight reattachment locations cannot be determined.

To convert the flight-measured heat flux into Stanton number, temperatures at the locations of the heat-flux microsensors were estimated by linearly interpolating between the two nearest thermocouples. Uncertainty in St was calculated by propagating uncertainties in freestream and total properties from Ref. [31] through Eq. 1. Figure 32 presents St profiles from the ANDLM6QT, computations, and flight at matched Re_L. Off-wall measured separation and reattachment locations are indicated for the ground-test results. As shown by VULCAN-CFD computations, the higher ground-test M_∞ results in lower St on the cone. On the conical forebody, St measured in the ANDLM6QT and in flight by the heat-flux microsensors agrees well with their corresponding computations. This is true both up- and downstream of separation. The separation locations, however, differ (Table 5).

On the flare, St in flight was 2–3× that measured in the ANDLM6QT, and also exceeded the turbulent computations. Several hypotheses for this difference have been considered:

- The nonzero angle of attack does not adequately explain the difference. Averaging heat flux over less than a full rotation period shows that the difference in heating between the windward and leeward sides is much less than the difference between flight and ground test.

- As noted above, the heat flux calculated from the thermocouples is suspected to be erroneous. If the front-face thermocouple yielded lower-than-true temperatures, which were then used to calculate Stanton number (along with heat flux from the HFMs), then the flight St would be erroneously high.
- The wall-to-stagnation temperature ratio was much lower in flight than in the ground tests. This difference alters the flow's stability, potentially causing earlier reattachment and/or shorter transition length in flight, thereby reaching (and exceeding) the turbulent heating rate farther upstream.‡
- Turbulent overshoot was experienced in flight, and the flare length was not long enough to recover the turbulent heating rate [95].

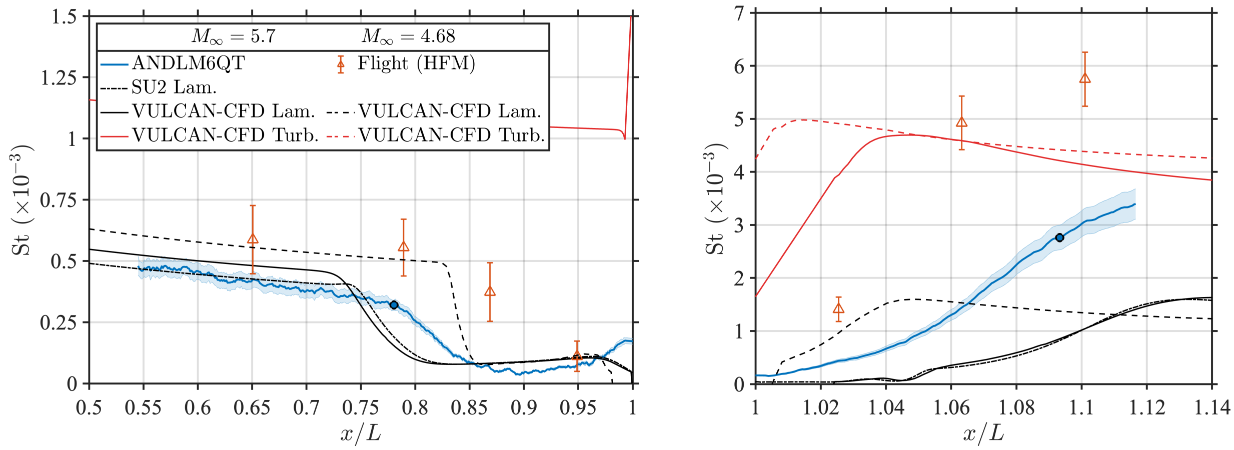

(a) Cone. **(b) Flare.**

Fig. 32 St**, ANDLM6QT matched** Re_L **= 2.4.**

Heating on the forebody in the AFRL M6LT is slightly lower than what VULCAN-CFD predicts (Fig. 33). The computed separation locations are upstream of their corresponding experimental results. Separation at the best-matching AFRL M6LT condition occurred at $x/L = 0.89$, within the range indicated by the flight-test instrumentation. The earlier reattachment in the AFRL M6LT than the ANDLM6QT gives a qualitatively more similar heating on the flare, although St remains almost 2× higher in flight.

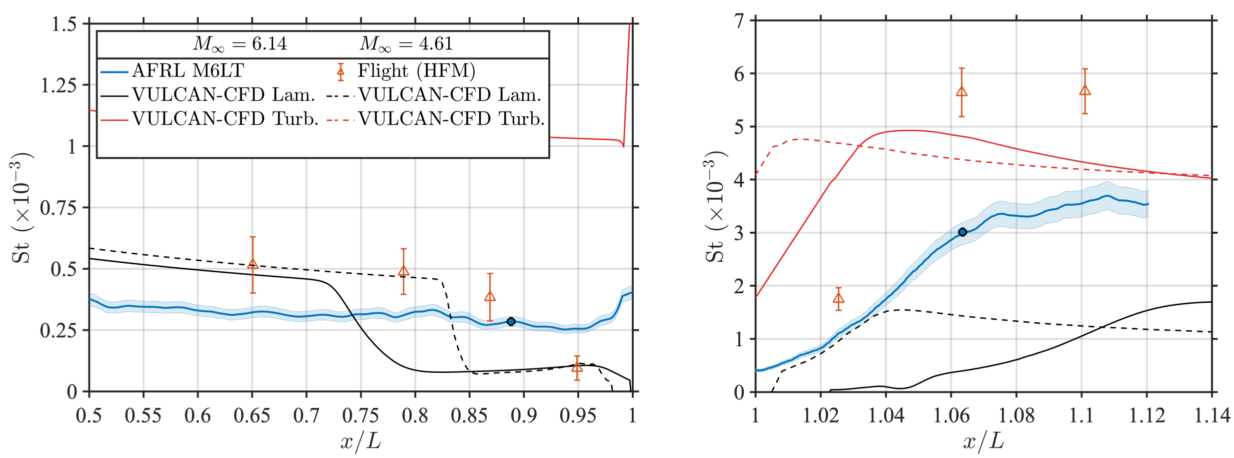

(a) Cone. **(b) Flare.**

Fig. 33 St**, AFRL matched** Re_L **= 2.8.**

‡The computations assumed a uniform wall temperature on the cone and flare. This is a reasonable approximation to the ground-test data (from short-duration wind tunnels), which exhibited a < 10 K difference between the cone and flare surface temperatures. However, flare temperatures in flight exceeded forebody temperatures by ≈ 100 K.

Table 5 SWBLI characteristics.

Source	M_∞	Flare Boundary-Layer State	x_s/L	x_r/L
ANDLM6QT	5.7	Transitional	0.78	1.09
SU2 (ground)	5.7	Laminar	0.7587	1.1180
VULCAN-CFD (ground)	5.7	Laminar	0.7479	1.1261
Flight	4.68	Transitional	0.79–0.95	–
VULCAN-CFD (flight)	4.68	Laminar	0.8718	1.0572
AFRL M6LT	6.14	Transitional	0.89	1.06
VULCAN-CFD (ground)	6.14	Laminar	0.7404	1.1264
Flight	4.61	Transitional	0.79 –0.95	–
VULCAN-CFD (flight)	4.61	Laminar	0.8481	1.0572

More Re_L-matched flight- and ground-test heating profiles are presented in Fig. 34. In each case, the boundary layer on the cone is laminar at separation. The separation location in flight is $0.87 < x_s/L < 0.97$, except for $Re_L = 0.91 \times 10^6$ and 1.8×10^6, where separation is further upstream, $0.79 < x_s/L < 0.87$. This trend is consistent with the ground tests, in which a lower Re_L resulted in earlier separation. For $Re_L = 0.91 \times 10^6$ to 1.8×10^6, the farthest downstream heat-flux sensor experiences highest heating. Without a discernible local maximum, the reattaching boundary layer is inferred to be transitional. For $Re_L \gtrapprox 2.9 \times 10^6$, maximum heating is indicated by a sensor other than the farthest downstream, indicating the flare boundary layer is at the end of transition. For $Re_L \gtrapprox 4.9 \times 10^6$, the farthest upstream flare heat-flux sensor experiences highest heating. The upstream movement of peak St indicates the separation bubble is shrinking, as in the ground tests. Within the precision afforded by the coarse flight-test instrumentation, the reattachment locations in flight coincide with those measured in the ANDLM6QT and AFRL M6LT.

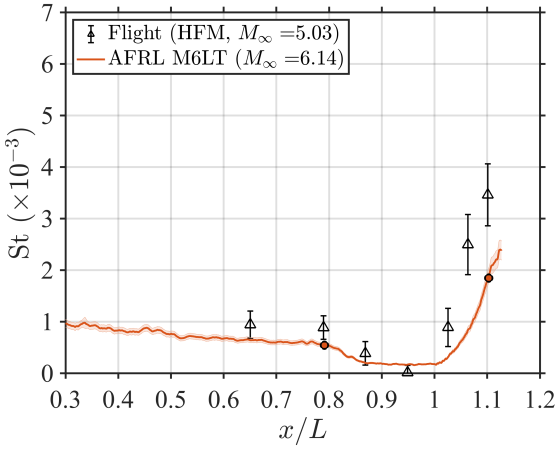

(a) $Re_L = 0.91 \times 10^6$.

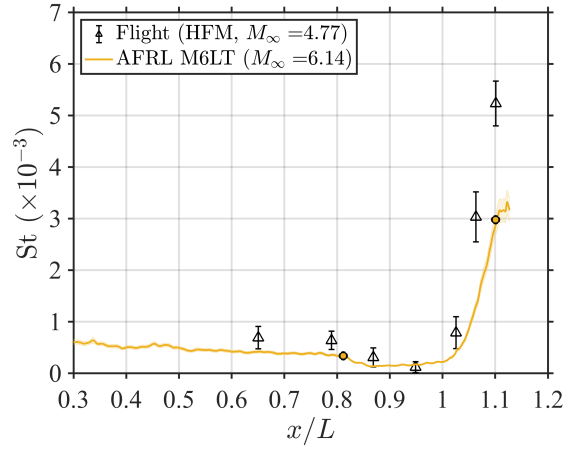

(b) $Re_L = 1.8 \times 10^6$.

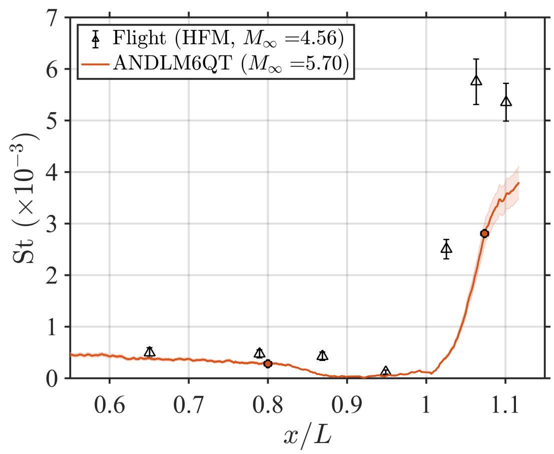

(c) $Re_L = 3.1 \times 10^6$.

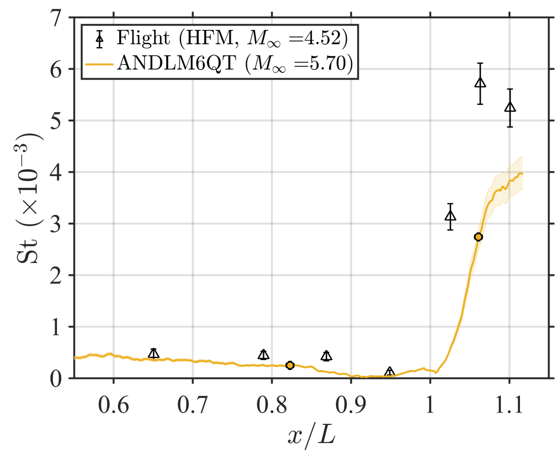

(d) $Re_L = 3.4 \times 10^6$.

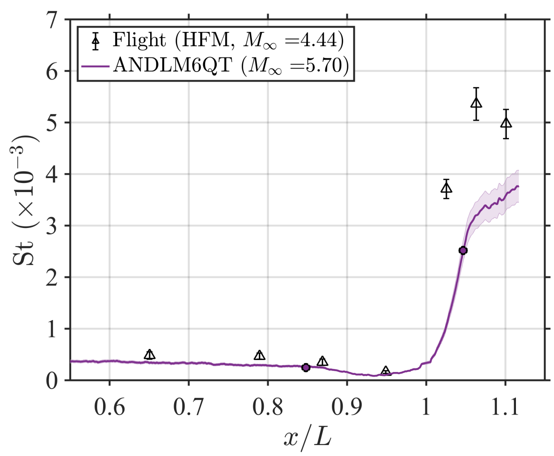

(e) $Re_L = 4.0 \times 10^6$.

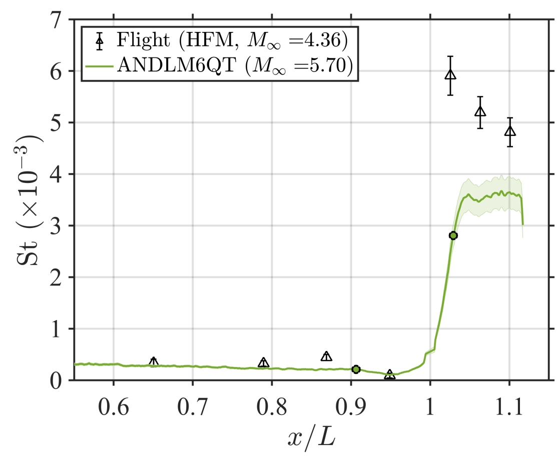

(f) $Re_L = 4.9 \times 10^6$.

Fig. 34 Effect of Re_L on St in flight- and ground-test.

IX. Conclusions

Coordinated computational and experimental investigations sought to better understand flare-induced transitional SWBLIs and ROTEX-T flight-test results. Experiments at nominally zero degrees angle of attack were carried out in the AFOSR–Notre Dame Large Mach-6 Quiet Tunnel and AFRL Mach-6 Ludwieg Tube. In the former, high resolution background-oriented schlieren and infrared thermography measurements were made at freestream unit Reynolds numbers from 5.8×10^6 to 12.2×10^6 m^{-1}. In the AFRL M6LT, high-speed self-aligned focusing schlieren, infrared thermography, and focused laser differential interferometry measurements were made at freestream unit Reynolds numbers from 2.2×10^6 m^{-1} to 24.7×10^6 m^{-1}. These measurements permitted identification of the separation and reattachment locations, as well as determination of the flow state at each.

Laminar separation was present for all Re_∞ tested in the ANDLM6QT except when a sharp nose was instrumented at the highest unit Reynolds number, 12.2×10^6 m^{-1}. For this specific condition, a subtle rise in St, rather than a decrement, indicated a transitional boundary layer on the cone. For an incoming laminar boundary layer, the point prior to a decrement in St correlated excellently with off-wall measurements. For freestream unit Reynolds numbers less than 10×10^6 m^{-1}, the boundary layer on the flare was transitional. The continuous rise in heating, with no discernible peak in St, did not allow for accurate determination of reattachment from surface measurements alone, but off-wall measurements identified reattachment unambiguously. Quantitative, high-resolution density fields agreed very well with the computations. The wall-normal density gradients were used to determine the boundary-layer edge and shear-layer locations. Computations demonstrated this definition of boundary-layer thickness – which is comparatively easy to measure with BOS – was very close to the wall-normal location of maximum stagnation enthalpy, which is frequently used to define the boundary-layer edge in computations.

The wider range of Reynolds numbers tested in the AFRL M6LT led to a greater variety of scenarios. At the lowest Re_∞, early separation meant the shear layer did not reattach on the flare. At high Re_∞, the turbulent boundary layer resisted separation. Transitional reattachment was observed at moderate Re_∞. When the incoming boundary layer was not laminar, the SAFS measurements showed no sign of a separation bubble. The general trends in heating were similar to the ANDLM6QT results, lower Re_∞ resulted in a transitional reattaching boundary-layer until a discernible peak in St occurred at a high enough Re_∞. The larger-radius nose delayed boundary-layer transition significantly, to $Re_\infty > 24.7 \times 10^6$ m^{-1}). Lower Re_∞, between 2.3×10^6 and 6.8×10^6 m^{-1}, resulted in a fully laminar shear layer that did not reattach.

The results of flight test, ground tests, and computations were compared at two matched length Reynolds numbers, one each for ANDLM6QT and AFRL M6LT experiments, for which the boundary layer was laminar at separation. Ground tests indicated later separation than computational results; separation in flight was later than both. Differences between computation and experiment are attributed to the limitations of steady, axisymmetric simulations, which leaves out relevant physics driving instability of a laminar separation bubble. Direct Numerical Simulation of this flow is in progress. Previous analysis of the flight data had not assessed reattachment location or the flow state upon reattachment. Thanks to the insights gained from the coordinated, on- and off-wall ground-test measurements with high spatial resolution, these evaluations have now been made.

Acknowledgements

The authors thank Amanda Chou and Andrew Leidy for discussions pertaining to this work. Jonathan Davami is supported by a University of Notre Dame Dean's Fellowship. Anton Scholten and Pedro Paredes are supported by the U. S. Office of Naval Research under award numbers N00014-20-1-2261 and N00014-23-1-2456. Pedro Paredes is also partially supported by the Hypersonic Technology Project (HTP) under the NASA Aeronautics Research Mission Directorate (ARMD) and by the Air Force office of Scientific Research under award number FA9550-20-1-0023. The computational resources supporting this work were provided by the DoD High Performance Computing Modernization Program and the NASA LaRC K Cluster at the Langley Research Center. The work of Kamil Dylewicz, Vojtech Pezlar and Vassilis Theofilis is supported by the Air Force Office of Scientific Research under award number FA8655-23-1-7031 "Linear modal and non-modal instability analyses of high-speed laminar separated flow over complex geometries. Part II: The HIFiRE-1, ROTEX-T and Oberkampf vehicles" with Dr. Douglas Smith as Program Officer.

References

[1] Asma, C., Paris, S., and Tapsoba, M., "Transitional Shock-Wave Boundary Layer Interaction Over a Cone-Flare Model at Hypersonic Conditions," ESASP Paper 487, 2002. URL `https://adsabs.harvard.edu/full/2002ESASP.487..725A`.

[2] Holden, M. S., "Shock Interaction Phenomena in Hypersonic Flows," AIAA Paper 1998-2751, 1998. https://doi.org/10.2514/6.1998-2751.

[3] Benay, R., Chanetz, B., Mangin, B., Vandomme, L., and Perraud, J., "Shock Wave/Transitional Boundary-Layer Interactions in Hypersonic Flow," *AIAA Journal*, Vol. 44, No. 6, 2006. https://doi.org/10.2514/1.10512.

[4] Running, C., Juliano, T., Jewell, S., Borg, M., and Kimmel, R., "Hypersonic shock-wave/boundary-layer interactions on a cone/flare," *Experimental Thermal and Fluid Science*, Vol. 109, No. 109911, 2019. https://doi.org/10.1016/j.expthermflusci.2019.109911.

[5] Kimmel, R., and Poggie, J., "Transition on an Elliptic Cone at Mach 8," American Society of Mechanical Engineers ASME FEDSM97-3111, 1997. https://doi.org/10.2514/2.836.

[6] Babinsky, H., and Harvey, J. K., *Shock Wave-Boundary-Layer Interactions*, 1st ed., Cambridge University Press, 2011, Chap. 1, pp. 11–17. https://doi.org/10.1017/CBO9780511842757.

[7] Gaitonde, D. V., "Progress in Shock Wave/Boundary Layer Interactions," AIAA Paper 2013-2607, 2013. https://doi.org/10.2514/6.2013-2607.

[8] Davami, J., Amanda, C., Leidy, A., and Juliano, T. J., "Effect of Roughness on BOLT-1a Geometry Transition in Supersonic Flow," , January 2023. https://doi.org/10.2514/6.2023-3441.

[9] Anderson, J., *Modern Compressible Flow*, 4th ed., McGraw-Hill, New York, 2021, Chap. 10: Conical Flow, pp. 363–375.

[10] Holden, M. S., "Studies of the Mean and Unsteady Structure of Turbulent Boundary Layer Separation in Hypersonic Flow," AIAA paper 1991-1778, 1991. https://doi.org/10.2514/6.1991-1778.

[11] Pasha, A. A., Johnson, H. B., and Sinha, K., "Simulation of Hypersonic Shock/Turbulent Boundary-Layer Interactions Using Shock-Unsteadiness Model," *Journal of Propulsion and Power*, Vol. 28, No. 1, 2012. https://doi.org/10.2514/1.B34191.

[12] Gülhan, A., Neeb, D., Thiele, T., and Siebe, F., "Aerothermal Postflight Analysis of the Sharp Edge Flight Experiment-II," *Journal of Spacecraft and Rockets*, Vol. 53, No. 1, 2016. https://doi.org/10.2514/1.A33275.

[13] Thielicke, W., "Digital Particle Image Velocimetry Tool for MATLAB," , 2022. URL https://pivlab.blogspot.com.

[14] Benitez, E. K., Esquieu, S., Jewell, J. S., and Schneider, S. P., "Instability Measurements on an Axisymmetric Separation Bubble at Mach 6," AIAA Paper 2020-3072, June 2020. https://doi.org/10.2514/6.2020-3072.

[15] Lugrin, M., Nicolas, F., Severac, N., Tobeli, J. P., Beneddine, S., Garnier, E., Esquieu, S., and Bur, R., "Transitional Shockwave/Boundary Layer Interaction Experiments in the R2Ch Blowdown Wind Tunnel," *Exp Fluids*, Vol. 63, No. 46, 2022. https://doi.org/10.1007/s00348-022-03395-9.

[16] Leinemann, M., Radespiel, R., Muñoz, F., Esquieu, S., McKiernan, G., and Schneider, S. P., "Boundary Layer Transition on a Generic Model of Control Flaps in Hypersonic Flow," AIAA Paper 2019-1908, 1995. https://doi.org/10.2514/6.2019-1908.

[17] Garcia, M., Hoffman, E. N. A., LaLonde, E. J., Combs, C. S., Pohlman, M., Smith, C., Gragston, M. T., and Schmisseur, J. D., "Effects of Surface Roughness on Shock-Wave/Turbulent Boundary-Layer Interaction at Mach 4 over a Hollow Cylinder Flare Model," *Fluids*, Vol. 7, No. 9, 2022. https://doi.org/10.3390/fluids7090286.

[18] Stanfield, S. A., Kimmel, R. L., Adamczak, D., and Juliano, T. J., "Boundary-Layer Transition Experiment During Reentry of HIFiRE-1," *Journal of Spacecraft and Rockets*, Vol. 52, No. 3, 2015, pp. 637–649.

[19] Running, C., Juliano, T., Borg, M., and Kimmel, R., "Characterization of Post-Shock Thermal Striations on a Cone/Flare," *AIAA Journal*, Vol. 58, No. 5, 2020. https://doi.org/10.2514/1.J059095.

[20] Rajendran, L. K., Zhang, J., Bhattacharya, S., Bane, S. P., and Vlachos, P. P., "Uncertainty Quantification in Density Estimation from Background Oriented Schlieren (BOS) Measurements," 13th International Symposium on Particle Image Velocimetry, 2019. URL https://athene-forschung.unibw.de/doc/129319/129319.pdf.

[21] Labuda, D. A., "Schlieren Imaging and Flow Analysis on a Cone/Flare Model in the AFRL Mach 6 Ludwieg Tube Facility," *Air Force Institute of Technology Theses and Dissertations*, 2019. URL https://scholar.afit.edu/etd.

[22] Butler, C. S., and Laurence, S. J., "Transitional Hypersonic Flow Over Slender Cone/Flare Geometries," *Journal of Fluid Mechanics*, Vol. 949, No. A37-40, 2022. https://doi.org/10.1017/jfm.2022.769.

[23] Davami, J., Juliano, T. J., Scholten, A., and Paredes, P., "Hypersonic Shock-Wave/Boundary-Layer Interactions on the ROTEX-T Cone/Flare," , January 2023. https://doi.org/10.2514/6.2023-1436.

[24] Benitez, E., Borg, M. P., Scholten, A., Paredes, P., and Jewell, J. S., "Instability and transition onset downstream of a laminar separation bubble at Mach 6," *Journal of Fluid Mechanics*, Vol. 969, No. 11, 2023. https://doi.org/10.1017/jfm.2023.533.

[25] Benitez, E., Borg, M. P., Paredes, P., and Jewell, J. S., "Measurements of an axisymmetric hypersonic shear-layer instability on a cone-cylinder-flare in quiet flow," *Physical Review Fluids*, Vol. 8, No. 083903, 2023. https://doi.org/10.1103/PhysRevFluids.8.083903.

[26] Arnal, D., and Delery, J., "Laminar-Turbulent Transition and Shock Wave/Boundary layer interaction," *AIAA Journal of the Aerospace Sciences*, Vol. 28, No. 5, 2004. https://doi.org/10.2514/8.9002.

[27] Balakumar, P., Zhao, H., and Atkins, H., "Stability of Hypersonic Boundary Layers Over a Compression Corner," *AIAA Journal*, Vol. 43, No. 4, 2002. https://doi.org/10.2514/1.3479.

[28] Gülhan, A., Thiele, T., Siebe, F., Klingenberg, F., Kronen, R., Stamminger, A., Scheuerpflug, F., Kallenbach‡, A., and Jung, W., "Main Achievements of the Rocket Technology Flight Experiment ROTEX-T," 21st AIAA International Space Planes and Hypersonics Technologies Conference, 2017. https://doi.org/10.2514/6.2017-2208, URL 10.2514/6.2017-2208.

[29] Weihs, H., Longo, J., and Turner, J., "The Sharp Edge Flight Experiment SHEFEX II, a Mission Overview and Status," AIAA Paper 2008-2542, 2008. https://doi.org/10.2514/6.2008-2542.

[30] Franze, M., "SHEFEX II - A First Aerodynamic and Atmospheric Post-Flight Analysis," AIAA Paper 2016-0786, 2016. https://doi.org/10.2514/6.2016-0786.

[31] Thiele, T., Gülhan, A., and Oliver, H., "Instrumentation and Aerothermal Postflight Analysis of the Rocket Technology Flight Experiment ROTEX-T," *AIAA Journal of Spacecraft and Rockets*, Vol. 55, No. 5, 2018. https://doi.org/10.2514/1.A34129.

[32] InfraTec, "COSPAR International Reference Atmosphere (CIRA-86): Global Climatology of Atmospheric Parameters," CDEA Archive Dataset Collection, 2018. URL https://catalogue.ceda.ac.uk/uuid/4996e5b2f53ce0b1f2072adadaeda262.

[33] Lakebrink, M. T., Bowcutt, K. G., Winfree, T., Huffman, C. C., and Juliano, T. J., "Optimization of a Mach-6 Quiet Wind Tunnel Nozzle," *Journal of Spacecraft and Rockets*, Vol. 55, No. 2, 2018, pp. 315–321. https://doi.org/10.2514/1.A33794.

[34] Hoberg, E. M., and Juliano, T. J., "Freestream Characterization and Condensation Detection in the AFOSR–Notre Dame Large Mach-6 Quiet Tunnel," AIAA Paper 2023-1458, January 2023.

[35] Benitez, E. K., Esquieu, S., Jewell, J. S., and Schneider, S. P., "Separation Bubble Variation Due to Small Angles of Attack for an Axisymmetric Model at Mach 6," AIAA Paper 2021-0245, 2021. https://doi.org/10.2514/6.2021-0245.

[36] Sutherland, W., "The viscosity of gases and molecular force, London, Edinburgh," *Dublin Philos. Magaz. J. Sci.*, Vol. 36, 1893, p. 507–531. URL https://www.tandfonline.com/doi/abs/10.1080/14786449308620508.

[37] Running, C. L., Rataczak, J. A., Zaccara, M., Cardone, G., and Juliano, T. J., "A wrap-film technique for infrared thermography heat-transfer measurements in high-speed wind tunnels," *Experimental Thermal and Fluid Science*, Vol. 135, No. 110604, 2022, pp. 1–8. https://doi.org/10.1016/j.expthermflusci.2022.110604.

[38] InfraTec, "Infrared-Thermographic Camera ImageIR," User Manual, 2016. URL https://www.infratec-infrared.com/thermography/infrared-camera/imageir-8300-hp/.

[39] InfraTec, "Infrared-Thermographic Camera ImageIR," User Manual, 2021. URL https://www.infratec.eu/thermography/infrared-camera/imageir-9400/#product-flyer.

[40] Juliano, T. J., Adamczak, D., and Kimmel, R. L., "HIFiRE-5 Flight Test Results," *Journal of Spacecraft and Rockets*, Vol. 52, No. 3, 2015, pp. 650–663. https://doi.org/10.2514/1.A33142.

[41] Boyd, C. F., and Howell, A., "Numerical Investigation of One-Dimensional Heat-Flux Calculations," Tech. Rep. NSWCDD/TR-94/114, Dahlgren Division Naval Surface Warfare Center, Silver Spring, MD 20903-5640, October 1994. URL https://apps.dtic.mil/sti/citations/ADA286293.

[42] Rataczak, J. A., Running, C. L., and Juliano, T. J., "Verification of quantitative infrared thermography heat-flux measurements," *Experimental Thermal and Fluid Science*, Vol. 121, No. 110274, 2021, pp. 1–8. https://doi.org/10.1016/j.expthermflusci.2020.110274.

[43] Moisy, F., "PIVMat 4.20 A PIV Post-processing and Data Analysis Toolbox," MATLAB, 2021. URL https://www.mathworks.com/matlabcentral/fileexchange/10902-pivmat-4-20.

[44] Thielicke, W., and Stamhuis, E. J., "PIVlab – Towards User-friendly, Affordable and Accurate Digital Particle Image Velocimetry in MATLAB," , 2014. https://doi.org/10.5334/jors.bl.

[45] Thielicke, W., and Sonntag, R., "Particle Image Velocimetry for MATLAB: Accuracy and Enhanced Algorithms in PIVlab," *Journal of Open Research Software*, Vol. 9(1), 2017, p. 12. https://doi.org/10.5334/jors.334.

[46] Radon, J., "On the Determination of Functions from their Integrals along Certain Manifolds," *IEEE Transactions on Medical Imaging*, Vol. 5, No. 4, 1917, pp. 170–176. https://doi.org/10.1109/TMI.1986.4307775.

[47] Venkatakrishnan, L., and Meier, G. E. A., "Density Measurements using the Background Oriented Schlieren Technique," *Experiments in Fluids Paper*, Vol. 37, 2004, p. 237–247. https://doi.org/10.1007/s00348-004-0807-1.

[48] Saleh, B., *Introduction to Subsurface Imaging*, 1st ed., Cambridge University Press, 2012, Chap. 4, pp. 142–188. https://doi.org/10.1017/CBO9780511732577.

[49] Shepp, L., and Logan, B., "The Fourier Reconstruction of a Head Section," *Dahlgren Division Naval Surface Warfare Center, Silver Spring, MD 20903-5640*, Vol. 21, No. 3, 1974, pp. 21–43. https://doi.org/10.1109/TNS.1974.6499235.

[50] Davami, J., Juliano, T. J., Moreto, J. R., and Liu, X., "Reconstructing a Hypersonic Shock-Wave/Boundary-Layer Interaction using Parallel-Ray Omni-Directional Integration," , 2023.

[51] Rajendran, L., Zhang, J., Bane, S., and Vlachos, P., "Uncertainty-Based Weighted Least Squares Density Integration for Background-Oriented Schlieren," *Experiments in Fluids*, Vol. 61, No. 239, 2020, p. 61:239. https://doi.org/10.1007/s00348-020-03071-w.

[52] Hill, J., Borg, M., Benitez, E., Running, C., and Reeder, M., "Implementation of Self-Aligned Focusing Schlieren for Hypersonic Boundary Layer Measurements," AIAA Paper 2023-2438, 2023. https://doi.org/10.2514/6.2023-2438.

[53] Towne, A., Schmidt, O., and Colonius, T., "Spectral Proper Orthogonal Decomposition and its Relationship to Dynamic Mode Decomposition and Resolvent Analysis," *Journal of Fluid Mechanics*, Vol. 847, 2018, p. 821–867. https://doi.org/10.1017/jfm.2018.283.

[54] Smeets, G., and George, A., "Laser-Differential Interferometer Applications in Gas Dynamics," Tech. Rep. R136/75, Institut Saint-Louis, 1975. Translated by A. Goetz, DTIC citation ADA307458.

[55] Gladstone, J., and Dale, T., "Researches on the Refraction, Dispersion, and Sensitiveness of Liquids," *Proceedings of the Royal Society of London*, Vol. 12, 1863, p. 317–343. https://doi.org/10.1098/rspl.1862.0097.

[56] Gragston, M., Price, T., Davenport, K., Schmisseur, J., and Zhang, Z., "An m-by-n FLDI Array for Single-Shot, Multipoint Disturbance Measurements in High-Speed Flows," AIAA Paper 2021-0599, 2021. https://doi.org/10.2514/6.2021-0599.

[57] Benitez, E., Leger, T., Tufts, M., Borg, M., and Hill, J., "Hypersonic Transitional Boundary-Layer Profile using a Linear-Array FLDI," AIAA Paper 2023-4253, 2023. https://doi.org/10.2514/6.2023-4253.

[58] Litton, D., Edwards, J., and White, J., "Algorithmic Enhancements to the VULCAN Navier-Stokes Solver," 16th AIAA Computational Fluid Dynamics Conference, June 2003. https://doi.org/10.2514/6.2003-3979.

[59] Baurle, R., White, J., Drozda, T., and Norris, A., "VULCAN-CFD Theory Manual: Ver. 7.1.0," NASA TM-2020-5000766, 2020.

[60] Baurle, R., White, J., Drozda, T., and Norris, A., "VULCAN-CFD User Manual: Ver. 7.1.0," NASA TM-2020-5000767, 2020.

[61] Scholten, A., Paredes, P., Li, F., White, J., Baurle, R., and Choudhari, M., "Automatic Boundary-Layer Adaptation of Structured Grids in VULCAN-CFD," ICCFD11 Paper 2022-1304, 2022.

[62] Menter, F. R., "Two-Equation Eddy-Viscosity Turbulence Models for Engineering Applications." *AIAA Journal*, Vol. 32, No. 8, 1994, pp. 1598–1605.

[63] Venkatakrishnan, V., "Convergence to steady state solutions of the Euler equations on unstructured grids with limiters," *Journal of Computational Physics*, Vol. 118, No. 1, 1995, pp. 120–130.

[64] Tobak M., Peake D.J., "Topology of two-dimensional and three-dimensional separated flows." *AIAA paper*, Vol. 79, 1979, p. 1480.

[65] Dallman U., "Three-dimensional vortex structures and vorticity topology." *Fluid Dynamic Research*, Vol. 3, 1988, pp. 183–189.

[66] Délery, J., "Robert Legendre and Henri Werlé Toward the Elucidation of three-dimensional separation," *Annu. Rev. Fluid Mech.*, Vol. 33, 2001, pp. 129–154.

[67] Illingworth, C., "Steady flow in the laminar boundary layer of a gas," *Proceedings of the Royal Society of London. Series A. Mathematical and Physical Sciences*, Vol. 199, No. 1059, 1949, pp. 533–558.

[68] Levy, S., "Effect of large temperature changes (including viscous heating) upon laminar boundary layers with variable free-stream velocity," *Journal of the Aeronautical Sciences*, Vol. 21, No. 7, 1954, pp. 459–474.

[69] Lees, L., "Laminar heat transfer over blunt-nosed bodies at hypersonic flight speeds," *Journal of Jet Propulsion*, Vol. 26, No. 4, 1956, pp. 259–269.

[70] Lees, L., and Lin, C.-C., *Investigation of the stability of the laminar boundary layer in a compressible fluid*, 1115, National Advisory Committee for Aeronautics, 1946.

[71] Lees, L., "The stability of the laminar boundary layer in a compressible fluid," Tech. rep., NASA, 1947.

[72] Mack, L. M., "Boundary-layer linear stability theory," Tech. rep., California Inst of Tech Pasadena Jet Propulsion Lab, 1984.

[73] Mack, L. M., "Review of linear compressible stability theory," *Stability of time dependent and spatially varying flows*, Springer, 1987, pp. 164–187.

[74] Rayleigh, L., "On the instability of jets," *Proceedings of the London mathematical society*, Vol. 1, No. 1, 1878, pp. 4–13.

[75] Rayleigh, L., "On the stability, or instability, of certain fluid motions," *Proc. London Math. Soc.*, Vol. 9, 1880, pp. 57–70.

[76] Paredes, P., Scholten, A., Choudhari, M., Li, F., Benitez, E., and Jewell, J., "Boundary-Layer Instabilities Over a Cone-Cylinder-Flate Model at Mach 6," AIAA Paper 2022-0600, 2022. https://doi.org/10.2514/6.2022-0600.

[77] Paredes, P., Scholten, A., Choudhari, M., Li, F., Benitez, E., and Jewell, J., "Boundary-Layer Instabilities Over a Cone-Cylinder-Flate Model at Mach 6," *AIAA Journal*, Vol. 60, No. 10, 2022. https://doi.org/10.2514/1.J061829.

[78] Paredes, P., Choudhari, M., Li, F., Jewell, J., Kimmel, R., Marineau, E., and Grossir, G., "Nosetip bluntness effects on transition at hypersonic speeds: experimental and numerical analysis," *Journal of Spacecraft Rockets*, Vol. 56, No. 2, 2019. https://doi.org/10.2514/1.A34277.

[79] Chu, B.-T., "On the Energy Transfer to Small Disturbances in Fluid Flow (Part I)," *Acta Mechanica*, Vol. 1, No. 3, 1956, pp. 215–234. https://doi.org/10.1007/BF01387235.

[80] Mack, L. M., "Boundary layer stability theory," Tech. Rep. Jet Propulsion Laboratory Report 900-277, California Institute of Technology, Pasadena, CA, 1969.

[81] Saad, Y., "Variations of Arnoldi's method for computing eigenelements of large unsymmetric matrices," *Linear Algebra Applications*, Vol. 34, 1980, pp. 269–295. https://doi.org/10.1016/0024-3795(80)90169-X.

[82] Schrijer, F., and Scarano, F., "Experiments on Hypersonic Boundary Layer Separation and Reattachment on a Blunted Cone-Flare using Quantitative Infrared Thermography," 12th AIAA International Space Planes and Hypersonic Systems and Technologies, 2003. https://doi.org/10.2514/6.2003-6967.

[83] Heffneri, K., Chpoun, A., and J.C., "Experimenta1 Study of Transitional Axisymmetric Shock-Boundary Layer Interactions at Mach 5," AIAA 23rd fluid dynamics, plasmadynamics, and lasers conference, 1993. https://doi.org/10.2514/6.1993-3131.

[84] Johna, B., Surendranathb, S., Natarajanb, G., and Kulkarni, V., "Analysis of dimensionality effect on shock wave boundary layer interaction in laminar hypersonic flows," *International Journal of Heat and Fluid Flow*, Vol. 62B, 2021, pp. 375–385. https://doi.org/10.1016/j.ijheatfluidflow.2016.09.009.

[85] Becker, J., and Korycinski, P., "Heat Transfer and Pressure Distribution at a Mach Number of 6.8 on Bodies with Conical Flares and Extensive Flow Separation," Tech. Rep. RM L56F22, NACA, Apr. 1956. DTIC citation AD0274584.

[86] Lugrin, M., Beneddine, S., Leclercq, C., Garnier, E., and Bur, R., "Transition Scenario in Hypersonic Axisymmetrical Compression Ramp Flow," *Journal of Fluid Mechanics*, Vol. 949, No. A6-1 P0, 2021. https://doi.org/10.1017/jfm.2020.833.

[87] Gray, J. D., "Investigation of the Effect of Flare and Ramp angle on the Upstream Influence of Laminar and Transitional Reattaching Flows from Mach 3 to 7," Tech. rep., AEDC-TR-66-190, 1967.

[88] Pate, S. R., and Schueler, C. J., "Radiated aerodynamic noise effects on boundary-layer transition in supersonic and hypersonic wind tunnels," *AIAA Journal*, Vol. 7, No. 3, 1969, pp. 450–457. https://doi.org/10.2514/3.5128.

[89] Duan, L., Choudhari, M. M., Chou, A., Munoz, F., Radespiel, R., Schilden, T., Schröder, W., Marineau, E. C., Casper, K. M., Chaudhry, R. S., Candler, G. V., Gray, K. A., and Schneider, S. P., "Characterization of Freestream Disturbances in Conventional Hypersonic Wind Tunnels," *Journal of Spacecraft and Rockets*, Vol. 52, No. 2, 2018, pp. 357–368. https://doi.org/10.2514/1.A34290.

[90] Franko, K. J., and Lele, S. K., "Convergence to steady state solutions of the Euler equations on unstructured grids with limiters," *Journal of Fluid Mechanics*, Vol. 730, 2013, pp. 491–532. https://doi.org/10.1017/ifm.2013.350.

[91] Délery, J., *Three-dimensional separated flow topology*, Wiley, 2013.

[92] Theofilis, V., Hein, S., and Dallmann, U., "On the origins of unsteadiness and three-dimensionality in a laminar separation bubble," *Phil. Trans. R. Soc. Lond. A*, Vol. 358, 2000, pp. 3229–3246. https://doi.org/10.1098/rsta.2000.0706.

[93] Boin, J.-P., Robinet, J.-C., Corre, C., and Deniau, H., "3D steady and unsteady bifurcations in a shock-wave/laminar boundary layer interaction: a numerical study," *Theor. Comput. Fluid Dyn.*, Vol. 20, 2006, pp. 163–180.

[94] Knight, D., and Mortazavi, M., "Hypersonic Shock Wave Transitional Boundary Layer Interactions - A Review," AIAA Paper 2017-3124, 2017. https://doi.org/10.2514/6.2017-3124.

[95] Juliano, T. J., Jewell, J. S., and Kimmel, R. L., "HIFiRE-5b Boundary-Layer Transition Length and Turbulent Overshoot," *Journal of Spacecraft and Rockets*, Vol. 58, No. 2, 2021, pp. 265–283. https://doi.org/10.2514/1.A34856.